Rigid Sets and Coherent Sets in Realistic Ocean Flows

F Feppon, P F J Lermusiaux

Rigid Sets and Coherent Sets in Realistic Ocean Flows

F. Feppon[a,b], P.F.J. Lermusiaux[b,*]

[a] *Department of Mathematics, ETH Zürich, Rämistrasse 101, CH-8092 Zürich, Switzerland*
[b] *Department of Mechanical Engineering, Massachusetts Institute of Technology, 77 Mass. Ave., Cambridge, MA - 02139*

Abstract

This paper focuses on the extractions of Lagrangian Coherent Sets from realistic velocity fields obtained from ocean data and simulations, each of which can be highly resolved and non volume-preserving. Two classes of methods have emerged for such purpose: those relying on the flow map diffeomorphism associated with the velocity field, and those based on spectral decompositions of the Koopman or Perron-Frobenius operators. The two classes of methods are reviewed, synthesized, augmented, and compared numerically on three velocity fields. First, we propose a new "diffeomorphism-based" criterion to extract "rigid sets", defined as sets over which the flow map acts approximately as a rigid transformation. Second, we develop a matrix-free methodology that provides a simple and efficient framework to compute "coherent sets" with operator methods. Both new methods and their resulting *rigid sets* and *coherent sets* are illustrated and compared using three numerically simulated flow examples, including a realistic, submesocale to large-scale dynamic ocean current field in the Palau Island region of the western Pacific Ocean.

Keywords: LCS, Rigid sets, Koopman operator, Arnoldi Iterations, Ocean Modeling, Lagrangian transport, Realistic data
2010 MSC: 37C10, 37C05, 769R99

1. Introduction

The pioneering concept of Lagrangian Coherent Structures (LCS) has emerged [1] to offer visualization and understanding of material transport in time-dependent fluid flows. The terminology was born from direct observations of realistic flows and refers to the persistence of distinguished material sub-domains over time [2, 3, 4, 5]. Extracting LCS is expected to allow for improved Lagrangian hazard predictions; typical ocean applications include pollution tracking [6, 7, 8], search and rescue [9], or ecosystem characterizations [10, 11, 12]. To date, several definitions of LCS that do not fully coincide have been proposed [2, 13, 4, 14, 15, 16, 17, 18, 19], and there are as many computational methodologies to extract them from time-dependent (*non-autonomous*) velocity fields $\boldsymbol{v}(t, \boldsymbol{x})$. Here, the variable $\boldsymbol{x}$ denotes the spatial position over a two or three dimensional computational domain $\Omega \subset \mathbb{R}^n$ ($n = 2$ or $n = 3$). These approaches can be classified broadly into two categories [20].

The first category of methods [21, 22] focuses on the motion of individual particles whose location $\boldsymbol{x}(t)$ satisfies the Ordinary Differential Equation (ODE),

$$\begin{cases} \dot{\boldsymbol{x}} = \boldsymbol{v}(t, \boldsymbol{x}(t)) \\ \boldsymbol{x}(0) = \boldsymbol{x}_0, \end{cases} \tag{1}$$

or equivalently on the relevant feature of the flow map $\boldsymbol{\phi}^t : \Omega \to \mathbb{R}^n$ associated to (1) which is defined for any $\boldsymbol{x}_0 \in \Omega$ by $\boldsymbol{\phi}^t(\boldsymbol{x}_0) = \boldsymbol{x}(t)$. This first category of methods seeks simplified visualizations of the diffeomorphism

*Corresponding author
Email address: pierrel@mit.edu (P.F.J. Lermusiaux)

$\boldsymbol{\phi}^t$, which we refer to here as *diffeomorphism based* methods. The difficulty in displaying the vectorial function $\boldsymbol{\phi}^t : \mathbb{R}^n \to \mathbb{R}^n$ with a 2D or 3D plot is usually addressed by representing only exceptional features which are sufficient to offer a representative picture of its action over individual trajectories $\boldsymbol{x}(t)$. Several works have suggested that such relevant features are codimension one surfaces across which $\boldsymbol{\phi}^t$ exhibits a sharp gradient; particles that are located on either side of such surface have indeed largely diverging trajectories. Hence, these codimension one LCS (attracting, repelling, and elliptic LCS), extracted from Finite Time Lyapunov Exponent (FTLE) fields [17] or from tensor lines of the flow map Jacobian matrix $\mathrm{D}\boldsymbol{\phi}^t$ [23, 24, 25, 26], exhibit extremal properties of repulsion or attraction, ideally globally, or at least in the neighborhood of these surfaces. The aforementioned methods yield LCS that can be computed at a relatively low cost even for highly resolved velocity fields (by taking advantage of parallel computing for trajectory integrations). However these have also the flaw of offering hardly interpretable pictures when too many LCS are found in the domain [20]. For this reason, several other techniques (that we also refer to as diffeomorphism based methods) have been developed, such as braiding [19] or clustering [27]; see e.g. [28, 5] for more exhaustive reviews.

The second category of methods focuses on the action of advection onto passive tracer fields $f_0 \in L^2(\Omega)$, physically understood as weighted measures or density distributions of particles. This action is described by the functional operator $\boldsymbol{L} : f_0 \mapsto f_0 \circ (\boldsymbol{\phi}^t)^{-1}$, that maps the $L^2(\Omega)$ function f_0 to the advected distribution $f(t,\cdot) = f_0 \circ (\boldsymbol{\phi}^t)^{-1}$. The transported function $f(t,\cdot)$ is also the solution of the advection partial differential equation (PDE),

$$\begin{cases} (\partial_t + \boldsymbol{v}(t,\boldsymbol{x}) \cdot \nabla) f = 0 \\ \qquad\qquad f(0,\boldsymbol{x}) = f_0(\boldsymbol{x}). \end{cases} \tag{2}$$

We refer to the techniques falling into this second category as *operator based* methods, which have been introduced by Froyland et. al. [13, 29]. Different types of coherent structures, called "coherent sets", can be extracted from spectral decompositions of the operator $\boldsymbol{L}$ [30, 31, 32], which correspond to sets of simple geometry mixing slowly with their complement [33, 34]. In contrast with diffeomorphism based methods, this approach yields coherent structures that are subdomains and not codimension-one sets [31]. Furthermore, instead of exhibiting material coherence *uniformly*, coherent sets may allow large stretching within their boundaries but no mixing between each subsets of the partition, which yields a different picture of material transport than the first class of methods. Nevertheless, computing finite dimensional approximations of the functional operator $\boldsymbol{L} : L^2(\Omega) \to L^2(\boldsymbol{\phi}^t(\Omega))$ and their associated spectral decompositions (SVD or eigenvalue decompositions) is a challenging task, which is a priori much more costly than only estimating the invariant flow map diffeomorphism $\boldsymbol{\phi}^t : \Omega \to \mathbb{R}^n$. Hence most of the literature so far restricts the applications to rather low-resolution velocity fields [30] or to subregions of the working domain [35]. Specific techniques have been proposed in more recent works so as to treat highly resolved 2D or 3D velocity fields [36, 37], making use of finite element basis functions adapted to the advected domain $\boldsymbol{\phi}^t(\Omega)$.

This paper aims at synthesizing, improving and comparing computational methodologies from both *diffeomorphism* and *operator* based methods on three benchmark sets of "realistic" velocity data. The word "realistic" refers to velocity data that are gridded, potentially highly resolved, that may include inlets and outlets, and that are not necessary divergent free (volume-preserving), as is typically the case of high-dimensional realistic ocean current fields. The contributions of the paper are twofold.

In Section 3, we propose a new diffeomorphism based method that allows to characterize and extract very efficiently *rigid sets* (instead of codimension one surfaces). We define rigid sets as level-sets of a polar distance function, which correspond to subdomains over which the flow map behaves approximately as an isometry (the composition of a translation, rotation, and orthogonal symmetry). This formulation allows to rapidly visualize coherent regions of the domain at a desired scale and to detect configurations for which no such distinguished sets are found, *e.g.* when there is a uniform stretch everywhere in the domain.

Our second contribution is concerned with the application of operator based methods to realistic ocean current fields. In Section 4, we propose a new matrix-free numerical algorithm which allows to extract efficiently *coherent sets* from potentially highly resolved velocity data. Our technique uses Arnoldi iterations to compute eigenvectors of the transfer operator $\boldsymbol{L}$ without the need of storing the matrix associated to its

finite dimensional approximation. This approach does not rely on the construction of finite-element bases and can therefore be considered as an alternative to the methods of [36, 37]; crucially the same number of particles is used to compute FTLEs, rigid sets, or coherent sets with a resolution identical to that of the input velocity field.

The theoretical and methodological advances are illustrated and compared throughout the paper on three benchmark 2D numerical flows which are introduced and detailed beforehand in Section 2. These are the analytic double gyre flow of Shadden et. al. [17], a Navier-Stokes flow past a cylinder, and a high-dimensional data-driven simulation of a submesoscale to large-scale ocean current field in the Palau Island region of the western Pacific Ocean.

In what follows, a time dependent velocity field $\boldsymbol{v}(t, \boldsymbol{x})$ is considered, which is not necessarily a solution of the Navier-Stokes equations. Incompressibility, *i.e.* $\mathrm{div}(\boldsymbol{v}) = 0$, is satisfied approximately in the three examples considered in the sequel but is never a theoretical requirement.

2. Description of the three benchmark numerical flow fields

In Sections 3 and 4, the computation of rigid and coherent sets is numerically illustrated on three velocity fields examples: the analytic double-gyre flow, a Navier-Stokes Flow Past a Cylinder in the periodic regime, and a high-dimensional realistic submesoscale to large-scale ocean velocity field in the Palau Island region.

2.1. Analytic double-gyre

The double gyre flow is a classical 2D benchmark example for studying Lagrangian coherence of particle motions [17, 38, 4]. This flow consists of two vortices oscillating horizontally (Figure 1) and is commonly defined by the analytic expression of Shadden et al. [17] :

$$\boldsymbol{v}(t, \boldsymbol{x}) = (-\partial_y \psi, \partial_x \psi) \text{ with } \psi(\boldsymbol{x}, t; \omega) = A \sin[\pi f(x, t)] \sin(\pi y), \tag{3}$$

where $f(x, t) = \sigma \sin(\omega t) x^2 + (1 - 2\sigma \sin(\omega t))x$ and $\boldsymbol{x} = (x, y)$. The 2D domain is $\Omega = [0, 2] \times [0, 1]$ and the values considered for the parameters are $A = 0.1$, $\sigma = 0.1$ and $\omega = 2\pi/10$. The velocity values are given on a 512x256 grid and the flow is integrated between $t = 0$ and $t = 15$ by solving (1) with a Runge-Kutta 4 scheme for each point of the grid.

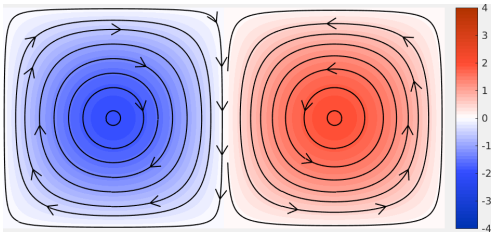

Figure 1: Streamlines and vorticity of the Double Gyre Flow at $t = 10$.

2.2. Flow Past a Cylinder

The second data set is obtained from a numerical simulation of a Flow Past a Cylinder solving the incompressible Navier-Stokes equations (Figure 2). The flow is set on a domain $\Omega = [0, 16] \times [0, 6]$ discretized with a 240×90 grid and a time step $\Delta t = 0.01$. The Reynolds number is Re=100. The cylinder is a disc of center $(x_c, y_c) = (4.5, 3)$ with radius $R = 0.5$. The flow enters the left side of the domain with a velocity $\boldsymbol{v} = (1, 0)$. Neumann boundary conditions are considered at the top and bottom walls, while the second normal derivative is set to $\partial^2 \boldsymbol{v}/\partial n^2 = 0$ at the right outflow. The flow is integrated by solving (1) on a non-dimensional time window $t \in [0, 10]$ on which the periodic regime is established (we discard the transient regime occurring at negative times). The ODE integration is performed with a Runge-Kutta 4 scheme using a linear interpolation of the velocity field in between time steps.

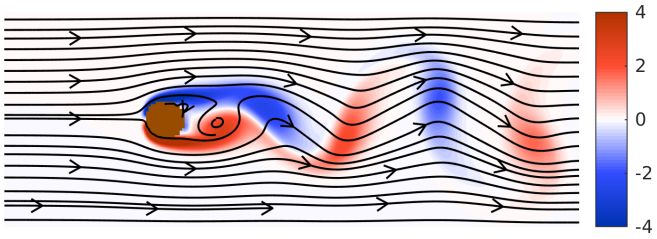

Figure 2: Streamlines and vorticity of the Flow Past a Cylinder Flow at $t = 0$ (transient regime discarded).

2.3. Realistic ocean current field in the Palau Island region

The third example is a high-dimensional numerical simulation of realistic ocean currents (Figure 3) in the Palau Island region of the western Pacific Ocean [39]. The ocean simulations were computed using the data-assimilative MIT MSEAS (Multidisciplinary Simulation, Estimation, and Assimilation System) modeling system [40, 41, 42], configured with implicit two-way nested computational domains. The domain utilized in the present examples spans a 420 km $\times$ 360 km region, with a 1/225° horizontal grid resolution and 70 optimized terrain-following vertical levels [43]. Initial conditions were downscaled from 1/12° HYCOM analyses (Hybrid Coordinate Ocean Model) [44] via optimization for our higher resolution coastlines and bathymetry [42]. The ocean simulations were forced with 1/4° GFS atmospheric fluxes from NCEP and with tidal forcing from the high resolution TPXO8-Atlas from OSU [45] with adjustments to our higher resolution geometry [46] and quadratic bottom drag. In the present Lagrangian studies, the size of the surface of the domain is 853x728. The total duration of the ocean currents utilized is 6 days corresponding to the period of May 8th – May 14th, 2015.

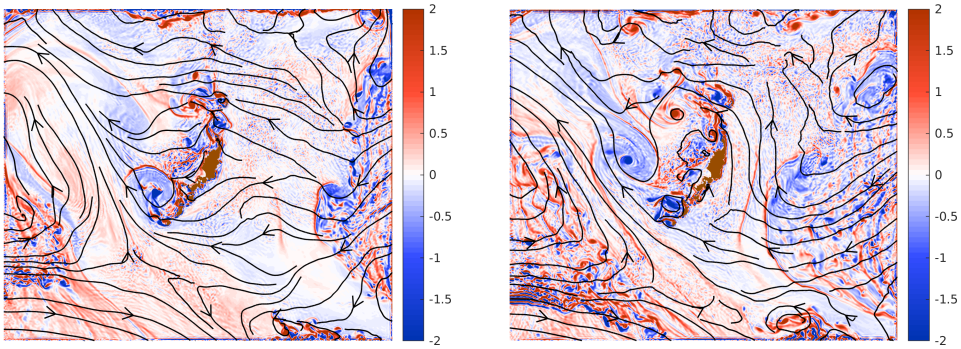

(a) Day 3 (b) Day 6

Figure 3: Streamlines and vorticity field around the Palau Island region at $t = 3$ and $t = 6$ days. The land is colored in brown.

This example is more challenging because (i) the resolution of this example is relatively high, (ii) the domain includes inlets, outlets, and an inner obstacle with complex geometry, and (iii) the surface flow field is complex with multi-scale currents, eddies, jets, wakes, tides, and waves [43], and is only approximately divergence-free, with a dynamic free-surface.

3. A diffeomorphism-based method: rigid sets from a polar distance

In this section, we propose a new diffeomorphism based method for the computation and visualization of LCSs. We define a polar distance functional from the singular value decomposition of the differential of the flow map. We then propose a simple criterion to define and extract *rigid sets* which are subdomains which preserves their shape when advected by a dynamic flow over a given time duration. The resulting method is evaluated numerically and compared to the more classically used FTLE field approaches [21, 7].

3.1. Notations: Singular Value Decomposition of the flow map Jacobian matrix

In the following, we use the notation $\boldsymbol{\phi}^{-t} = (\boldsymbol{\phi}^t)^{-1}$ for the inverse flow map between the instants 0 and t. The Singular Value Decomposition [47] of the differential of the forward (*resp.*, backward) flow map, $\mathrm{D}\boldsymbol{\phi}^t$ (*resp.*, $\mathrm{D}\boldsymbol{\phi}^{-t}$), at the position $\boldsymbol{x} \in \Omega \subset \mathbb{R}^n$ (*resp.*, $\boldsymbol{y} \in \boldsymbol{\phi}^t(\Omega) \subset \mathbb{R}^n$) is denoted by,

$$\mathrm{D}\boldsymbol{\phi}^t(\boldsymbol{x}) = \sum_{i=1}^{n} \sigma_i^t(\boldsymbol{x}) \boldsymbol{\eta}_i^t(\boldsymbol{x}) \boldsymbol{\xi}_i^{tT}(\boldsymbol{x}), \quad \mathrm{D}\boldsymbol{\phi}^{-t}(\boldsymbol{y}) = \sum_{i=1}^{n} \sigma_i^{-t}(\boldsymbol{y}) \boldsymbol{\eta}_i^{-t}(\boldsymbol{y}) \boldsymbol{\xi}_i^{-tT}(\boldsymbol{y}), \tag{4}$$

where singular values are assumed to be given in a decreasing order, (*i.e.* $\sigma_1^t(\boldsymbol{x}) \geq \sigma_2^t(\boldsymbol{x}) \geq \ldots \geq \sigma_n^t(\boldsymbol{x}) > 0$), and singular vectors form two orthonormal basis of $\mathbb{R}^n$. It is recalled that singular vectors and singular values of $\mathrm{D}\boldsymbol{\phi}^t$ (resp., $\mathrm{D}\boldsymbol{\phi}^{-t}$) can be obtained from the eigenvectors and eigenvalues of the symmetric Cauchy Green tensor $\mathrm{D}\boldsymbol{\phi}^t(\boldsymbol{x})^T \mathrm{D}\boldsymbol{\phi}^t(\boldsymbol{x})$ (resp., $\mathrm{D}\boldsymbol{\phi}^{-t}(\boldsymbol{y})^T \mathrm{D}\boldsymbol{\phi}^{-t}(\boldsymbol{y})$) [47, 4]. Any definition of LCS based on these spectral invariant satisfy the "objectivity" requirement as defined by Haller in [4]: all quantities derived from these singular values and vectors are independent under an Euclidean change of coordinates and hence of a particular reference frame.

In this context, right singular vectors $\boldsymbol{\xi}_i^t(\boldsymbol{x})$ of the differential $\mathrm{D}\boldsymbol{\phi}^t(\boldsymbol{x})$ of the forward flow map correspond to the directions in the initial domain characterized by maximal stretching of a fluid parcel located around the position $\boldsymbol{x}$. A local perturbation initially aligned along the right singular vector $\boldsymbol{\xi}_i^t(\boldsymbol{x})$ is stretched by the factor $\sigma_i^t(\boldsymbol{x})$ and rotated to align with the corresponding matching left singular vector $\boldsymbol{\eta}_i^t(\boldsymbol{x})$, as it is directly visible from the equality $\mathrm{D}\boldsymbol{\phi}^t(\boldsymbol{x})\boldsymbol{\xi}_i^T(\boldsymbol{x}) = \sigma_i^t(\boldsymbol{x})\boldsymbol{\eta}_i^t(\boldsymbol{x})$. Naturally, the same properties hold for the backward flow map $\boldsymbol{\phi}^{-t}$ by inverting initial and advected domain. It is useful to bear in mind the duality between the SVD of the forward and backward flow maps as stated in [48, 49, 14, 20]:

Proposition 1. *The differential* $\mathrm{D}\boldsymbol{\phi}^t(\boldsymbol{x})$ *of the flow map and the differential* $\mathrm{D}\boldsymbol{\phi}^{-t}$ *of the inverse flow map are related by the formula* $\mathrm{D}\boldsymbol{\phi}^{-t} = (\mathrm{D}\boldsymbol{\phi}^t)^{-1} \circ \boldsymbol{\phi}^{-t}$. *This implies that the Singular Value Decomposition of* $\mathrm{D}\boldsymbol{\phi}^{-t}$ *is given by*

$$(\mathrm{D}\boldsymbol{\phi}^{-t})(\boldsymbol{y}) = \sum_{i=1}^{n} \sigma_i^t(\boldsymbol{\phi}^{-t}(\boldsymbol{y}))^{-1} \boldsymbol{\xi}^t(\boldsymbol{\phi}^{-t}(\boldsymbol{y})) \boldsymbol{\eta}^{tT}(\boldsymbol{\phi}^{-t}(\boldsymbol{y})).$$

In other words:

- *The* singular values *of* $\mathrm{D}\boldsymbol{\phi}^{-t}$ *are inverse of those of* $\mathrm{D}\boldsymbol{\phi}^t$ *advected backward in time:*

$$\sigma_i^{-t}(\boldsymbol{y}) = \sigma_{n-i+1}^t(\boldsymbol{\phi}^{-t}(\boldsymbol{y}))^{-1}.$$

- *The* right (resp., left) singular vectors *of* $\mathrm{D}\boldsymbol{\phi}^{-t}$ *are the corresponding* left (resp., right) singular vectors *of* $\mathrm{D}\boldsymbol{\phi}^t$ *advected backward in time:*

$$\boldsymbol{\xi}_i^{-t}(\boldsymbol{y}) = \boldsymbol{\eta}_{n-i+1}^t(\boldsymbol{\phi}^{-t}(\boldsymbol{y}))$$
$$\boldsymbol{\eta}_i^{-t}(\boldsymbol{y}) = \boldsymbol{\xi}_{n-i+1}^{-t}(\boldsymbol{\phi}^{-t}(\boldsymbol{y})).$$

It is recalled that the *forward* and *backward FTLE field* on the time window $[0, t]$, denoted respectively FTLE^t and FTLE^{-t}, are defined by a logarithmic rescaling of the maximal singular values $\sigma_1^t(\boldsymbol{x})$ and $\sigma_1^{-t}(\boldsymbol{y})$:

$$\mathrm{FTLE}^t(\boldsymbol{x}) = \frac{\log(\sigma_1^t(\boldsymbol{x}))}{t}, \qquad \mathrm{FTLE}^{-t}(\boldsymbol{y}) = \frac{\log(\sigma_1^{-t}(\boldsymbol{y}))}{t}. \tag{5}$$

These quantities estimate the local maximum stretch experienced by a fluid parcel or, in other words, the local Lipschitz regularity of the flow map. Ridges of the forward and backward FTLEs, *i.e.* lines where the FTLE is locally maximal, have been used to define repelling and attracting LCS [17]. If the domain is two-dimensional and the velocity field is divergent free, $\mathrm{div}(\boldsymbol{v}) = 0$, then Proposition 1 implies that the forward FTLE is the backward FTLE (a quantity defined on the advected domain) advected backward in time. Haller [4] suggested that LCS can be defined as integral curves of vector fields obtained from the singular

vectors $\boldsymbol{\xi}_t^i(\boldsymbol{x})$ or $\boldsymbol{\xi}_i^{-t}(\boldsymbol{y})$. Indeed, these curves are locally most repelling when allowing local deformations [3]. Nevertheless, this approach does not yield globally coherent structures since a LCS can be drawn from every point of the domain, and it is sometimes unclear how to retain the most influential ones. In [4], Haller proposes to select the curves that go along global maxima of the FTLE field, but it is not a priori guaranteed that a globally maximizing property is maintained all the way along the curve. Other useful variants of this approach have been considered in [24] as well as some instantaneous techniques [26], valid for small integration times or for autonomous systems.

3.2. Definition of rigid sets from the polar distance

We now propose a simple definition of coherent structures based on the singular decomposition of the differential of the flow map that addresses some of the above concerns. Our criterion allows to extract coherent subregions instead of codimension one surfaces. The idea is based on the following theorem which is a well known results of continuum mechanics [50, 51]:

Theorem 1. *Suppose that $\boldsymbol{\phi}^t$ is a transformation whose differential is an orthogonal matrix at any point of the domain Ω, namely*

$$\forall \boldsymbol{x} \in \Omega, \mathrm{D}\boldsymbol{\phi}^t(\boldsymbol{x})^T \mathrm{D}\boldsymbol{\phi}^t(\boldsymbol{x}) = I. \tag{6}$$

Then $\boldsymbol{\phi}^t$ is an isometry on Ω: $\mathrm{D}\boldsymbol{\phi}^t(\boldsymbol{x}) = P$ is a an element of the group $\mathcal{O}_n$ of n-by-n orthogonal matrices $P \in \mathcal{O}_n$ (independent of $\boldsymbol{x}$ and satisfying $P^T P = I$) and $\boldsymbol{\phi}^t$ is the composition of P with a uniform translation:

$$\forall \boldsymbol{x} \in \Omega, \boldsymbol{\phi}^t(\boldsymbol{x}) = \boldsymbol{\phi}^t(\boldsymbol{x}_0) + P(\boldsymbol{x} - \boldsymbol{x}_0).$$

The condition (6) states that the singular values of $\mathrm{D}\boldsymbol{\phi}^t$ are equal to one: $\sigma_i^t(\boldsymbol{x}) = 1$ for any $\boldsymbol{x} \in \Omega$. Theorem 1 suggests that a way to quantify how far the flow map $\boldsymbol{\phi}^t$ is from being a rigid transformation can be done by measuring how far the Jacobian matrix $\mathrm{D}\boldsymbol{\phi}^t(\boldsymbol{x})$ is from being an orthogonal matrix at every point. It turns out that John (1961) has showed that Theorem 1 is "stable under perturbations" in the following sense:

Theorem 2 (John [52], see also chapter 5, Theorem. 2.2 in [53])**.** *Let $B(\boldsymbol{x}_0, \rho) \subset \Omega$ be the ball centered at $\boldsymbol{x}_0$ and of radius ρ. Assume that there exists $\epsilon > 0$ such that*

$$\forall \boldsymbol{x} \in B(\boldsymbol{x}_0, \rho), \forall 1 \leq i \leq n, \, |\sigma_i^t(\boldsymbol{x}) - 1| \leq \epsilon,$$

where $\sigma_i^t(\boldsymbol{x}) = \sigma_i^t(\mathrm{D}\boldsymbol{\phi}^t(\boldsymbol{x}))$ is the i-th singular value of the Jacobian matrix $\mathrm{D}\boldsymbol{\phi}^t(\boldsymbol{x})$. Then there exists a constant C dependent only of the dimension n of $\mathbb{R}^n$ and an orthogonal matrix P independent of $\boldsymbol{x}$ such that $\boldsymbol{\phi}^t$ is close to be a rigid transformation on $B(\boldsymbol{x}_0, \rho)$:

$$\forall \boldsymbol{x} \in B(\boldsymbol{x}_0, \rho), ||\boldsymbol{\phi}^t(\boldsymbol{x}) - \boldsymbol{\phi}^t(\boldsymbol{x}_0) - P(\boldsymbol{x} - \boldsymbol{x}_0)|| \leq C\rho\epsilon.$$

Based on the previous ideas, we can propose a definition of rigid sets.

Definition 1. A set $\mathcal{A}_{rigid}$ is called *rigid* between the instants 0 and t if the restriction of flow map $\boldsymbol{\phi}^t$ to $\mathcal{A}_{rigid}$ is close to be a rigid transformation (the composition of a rotation, translation, and orthogonal symmetry), namely if there exists $\boldsymbol{x}_0 \in \Omega$ and $P \in \mathcal{O}_n$ such that,

$$\boldsymbol{\phi}^t(\mathcal{A}_{rigid}) \simeq \{\boldsymbol{x}_0 + P(\boldsymbol{x} - \boldsymbol{x}_0) \,|\, \boldsymbol{x} \in \mathcal{A}_{rigid}\}.$$

Remark 1. Orthogonal symmetries are allowed because large stretching of $\mathcal{A}_{rigid}$ can occur at intermediate times $0 < s < t$, which may deform the shape of $\mathcal{A}_{rigid}$ in such a way $\mathrm{D}\boldsymbol{\phi}^t(x) \simeq P$ at the final time t for an isometry satisfying $P \in \mathcal{O}_n$ with $\det(P) = -1$.

From Theorem 2, *rigid sets* are subdomains over which the singular values $(\sigma_i^t(\boldsymbol{x}))_{1 \leq i \leq n}$ of $\mathrm{D}\boldsymbol{\phi}^t$ remain close to one, according to a "distance" $\mathcal{P}(\mathrm{D}\boldsymbol{\phi}^t)$ to be defined. For example, the distance considered in

Theorem 2 is $\max_{1\leq i\leq n}|\sigma_i^t(\boldsymbol{x})-1|$. From the equivalence of norms in finite dimension, we rather consider the following quantity for our numerical applications:

$$\mathcal{P}(\mathrm{D}\boldsymbol{\phi}^t)(\boldsymbol{x})=\left(\sum_{i=1}^{n}(1-\sigma_i^t(\boldsymbol{x}))^2\right)^{\frac{1}{2}}. \tag{7}$$

This quantity can be showed to be equal to the Euclidean distance between the matrix $\mathrm{D}\boldsymbol{\phi}^t$ and its projection $P(\boldsymbol{x})$ onto the group of n-by-n orthogonal matrices $\mathcal{O}_n$:

$$\mathcal{P}(\mathrm{D}\boldsymbol{\phi}^t)(\boldsymbol{x})=||\mathrm{D}\boldsymbol{\phi}^t(\boldsymbol{x})-P(\boldsymbol{x})||=\inf_{P\in\mathcal{O}_n}||\mathrm{D}\boldsymbol{\phi}^t(\boldsymbol{x})-P||.$$

The projection $P(\boldsymbol{x})$ is also the unique matrix $P(\boldsymbol{x})\in\mathcal{O}_n$ occuring in the polar decomposition $\mathrm{D}\boldsymbol{\phi}^t=P(\boldsymbol{x})S(\boldsymbol{x})$ with $S(\boldsymbol{x})$ symmetric definite positive (see e.g. [54, 55]). For this reason, $\mathcal{P}$ is referred to as a *polar distance* in the present paper, because it measures the distance between a matrix and its polar part (see also [56]). Rigid sets $\mathcal{A}_{rigid}^{\epsilon,t}$ are defined from a simple threshold on the polar distance.

Definition 2. For a given $\epsilon>0$, the ϵ-rigid sets of $\boldsymbol{\phi}^t$ are the connected components of the set $\mathcal{A}_{rigid}^{\epsilon,t}$ defined by:

$$\mathcal{A}_{rigid}^{\epsilon,t}=\{\boldsymbol{x}\in\Omega|\mathcal{P}(\mathrm{D}\boldsymbol{\phi}^t)(\boldsymbol{x})\leq\epsilon\}. \tag{8}$$

The parameter ϵ allows for some tolerance over the scale at which one seeks the rigidity. Connected components of $\mathcal{A}_{rigid}^{\epsilon}$ are transformed by $\boldsymbol{\phi}^t$ in an approximate rigid manner, with a possible stretching of magnitude of order $\epsilon T\rho$ where ρ is the characteristic length of the each component set.

Remark 2. In 2D, *i.e.* $n=2$, and for a divergence free field, this criterion can be related to a thresholding of the FTLE field: indeed, the relation $\sigma_1^t(\boldsymbol{x})\sigma_2^t(\boldsymbol{x})=1$ holds for all times t, which can be showed to imply

$$\{\boldsymbol{x}\in\Omega|\mathrm{FTLE}^t(\boldsymbol{x})\leq\log(1+\epsilon/\sqrt{2})/t\}\subset\mathcal{A}_{rigid}^{\epsilon,t}\subset\{\boldsymbol{x}\in\Omega|\mathrm{FTLE}^t(\boldsymbol{x})\leq\log(1+\epsilon)/t\}.$$

Hence ridges of the FTLE that delimit regions *where the FTLE field is small* may be considered as true boundaries of rigid sets. This addresses the limitations of the ability of FTLE fields to detect LCSs: examples given in [23] for which FTLE ridges are disqualified to be LCS, are also disqualified to be rigid sets, in the sense that FTLE values of these examples are high everywhere in the domain. In these cases, the flow map $\boldsymbol{\phi}^t$ exhibits uniformly high stretching which translates to high values of the polar distance $\mathcal{P}(\mathrm{D}\boldsymbol{\phi}^t)(\boldsymbol{x})$ everywhere in the domain and the proposed criterion (8) thus correctly disqualifies these regions from being rigid sets: $\mathcal{A}_{rigid}^{\epsilon,t}$ is empty for small ϵ, even if the FTLE field admits ridges. Such a relation between FTLEs and rigid sets is lost in 3D or for non-volume preserving velocity fields.

Remark 3. Exploiting the duality of Proposition 1, an alternative definition of the polar distance could be

$$\mathcal{P}(\mathrm{D}\boldsymbol{\phi}^t)(\boldsymbol{x})=\left(\sum_{i=1}^{n}\frac{(1-\sigma_i^t(\boldsymbol{x}))^2}{\sigma_i^t(\boldsymbol{x})}\right)^{\frac{1}{2}}. \tag{9}$$

An advantage of using (9) rather than (7) is an invariance when inverting the direction of the time window: $\mathcal{P}(\mathrm{D}\boldsymbol{\phi}^{-t})=\mathcal{P}(\mathrm{D}\boldsymbol{\phi}^t)\circ\boldsymbol{\phi}^{-t}$. With this definition, rigid sets obtained from the thresholding of equation (8) at time 0 coincide with those obtained at time t from a thresholding of the backward flow map advected backward in time:

$$\mathcal{A}_{rigid}^{\epsilon,t}=\{\boldsymbol{x}\in\Omega|\mathcal{P}(\mathrm{D}\boldsymbol{\phi}^t)(\boldsymbol{x})\leq\epsilon\}=\boldsymbol{\phi}^{-t}(\{\boldsymbol{y}\in\boldsymbol{\phi}^t(\Omega)|\mathcal{P}(\mathrm{D}\boldsymbol{\phi}^{-t})(\boldsymbol{y})\leq\epsilon\}).$$

3.3. Further criterion

It is possible to extend the definition of the polar distance and their resulting rigid sets by taking into account the evolution of a set $\mathcal{A}^{\epsilon,t}_{rigid}$ over the whole time window $[0,t]$ instead of only the initial and final times 0 and t, e.g. $\mathcal{A}^{\epsilon,t}_{rigid} := (\mathcal{P}^t)^{-1}([0,\epsilon])$ with,

$$\mathcal{P}^t(\boldsymbol{x}) := \frac{1}{T}\int_0^t \sum_{i=1}^{n} \frac{(1-\sigma_i^s(\boldsymbol{x}))^2}{\sigma_i^s(\boldsymbol{x})}\mathrm{d}s.$$

We refer to [57, 58] for detailed analyses and examples on this extended polar distance.

3.4. Numerical Results

For each of the three examples of Section 2, the logarithm of the polar distance $\log(\mathcal{P}(\mathrm{D}\boldsymbol{\phi}^t)(\boldsymbol{x})$ (eq. (7)) is plotted on Figure 4, and compared to the associated FTLE field on Figure 5. "Rigid sets" $\mathcal{A}^{\epsilon,t}_{rigid}$ (with $\epsilon = 1$) on which the flow map acts approximately as a rigid transformation are obtained as the blue regions. Since these flows are approximately divergence free, a clear analogy is visible between the polar distance and the FTLE field: on Figure 5, rigid sets correspond to the darkest regions of the FTLE field. Initial and final configurations of rigid sets obtained with such thresholding are visible on Figure 6 and identified with matching colors. These examples demonstrate that the thresholding criterion (8) may be used to identify key subregions that are advected in a rigid manner.

For the Double Gyre Flow of Section 2.1, we identify 4 rigid sets depicted with four different colors on Figure 6a. It is interesting to observe that the flow map behaves visibly as the composition of a rigid rotation, orthogonal symmetry, and of a translation on each of the connected rigid subregions, but these transformations may be different on each component. Surrounding regions are characterized by increased material stretching. More specifically, rigid sets of the left part of the domain (in *red* and *blue*) evolve according to the left vortex of the flow (Figure 1) in a clock-wise rotation. Furthermore, we observe that a symmetry along the vertical axis comes into play between each matching pairs of rigid sets. As is highlighted in [57], this emphasizes that our polar distance criterion (7) is able to determine shapes that remain similar between the initial and the final instants, but which may undergo severe stretching at intermediate times $t \in (0, 15)$ (otherwise only a rotation and a translation could possibly occur on each component because the sign of $\det(\mathrm{D}\boldsymbol{\phi}^t)$ remains positive). The remaining part of the flow is subject to large stretching, e.g. due to the high shear between the two vortices, and no other rigid set is identified.

For the Flow Past a Cylinder of Section 2.2, we identify 6 rigid sets depicted with matching colors on Figure 6b. Clearly, each of these sets move mainly according to a translation towards the right as prescribed by the incoming flow. The sets labeled in *red* and *blue* are however also subject to some rotation. The remaining part of the flow is subject to large stretching due to the periodic oscillations of the flow, or leaves the domain before the final recorded time $t = 10$.

Finally, prominent connected rigid components are less easily identified for the high-dimensional surface flow in the Palau Island region Section 2.3, due to the occurrence of rather large stretching and transport barriers in multiple locations of the domain, as a result of the complex submesoscale-to-large currents around and above the steep topography of the Palau Archipelago. This is in agreement with the forward FTLE field of Figure 5c. The thresholding of the polar distance (7) with $\epsilon = 1$ yields the black regions visible on Figure 6c. Examining how these various sub-regions evolve with the flow, we identified 6 regional sets whose shapes are approximately conserved from the initial to the final time. Despite the larger complexity of the flow, this analysis allows us to qualitatively identify the main coherent sets and describe their advective transport. The *yellow* set evolves according to a slight translation towards the northwest with almost no rotation. The *violet*, *brown* and *light green* set are only approximately translated towards the northwest, north-northwest, and north, respectively, as each undergo some east-west stretching. The *dark red* subdomain is subject to a significantly larger translation towards the northwest. The *dark green* subdomain is subjected to approximately the same translation towards the northwest but with a more significant rotation.

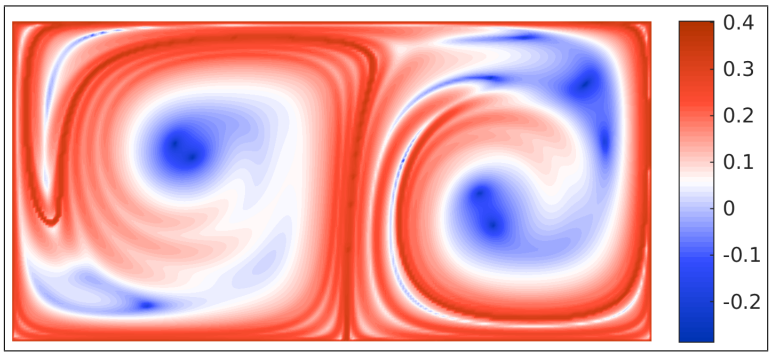

(a) Double Gyre Flow of Section 2.1(forward time, from $t = 0$ to $t = 15$)

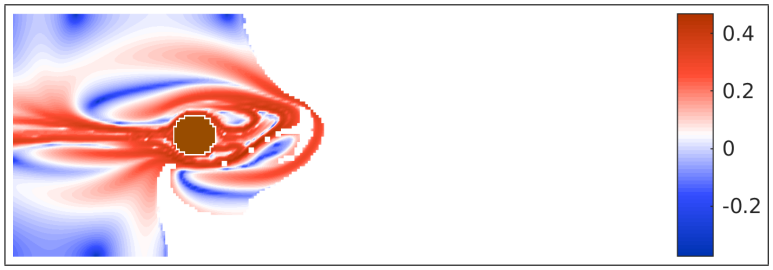

(b) Flow Past a Cylinder of Section 2.2 (forward time, from $t = 0$ to $t = 10$).

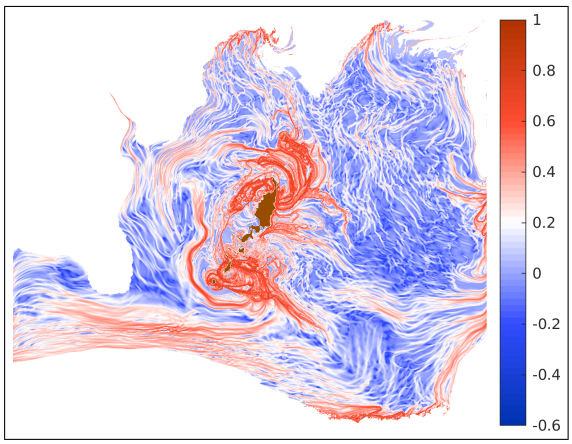

(c) Palau Island flow of Section 2.3 from May 8th 2015 (forward time, from $t = 0$ to $t = 6$ days), in day^{-1} (color scale).

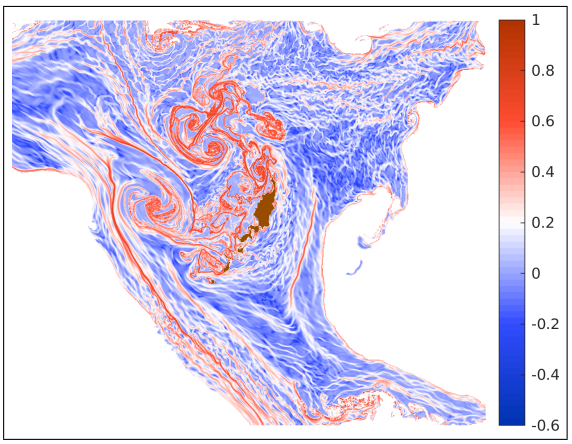

(d) Palau Island flow of Section 2.3 from May 14th 2015 (backward time, from $t = 6$ days to $t = 0$), in day^{-1} (color scale).

Figure 4: Plots of the logarithm of the polar distance $\log(\mathcal{P}(\mathrm{D}\boldsymbol{\phi}^t)(\boldsymbol{x}))/t$ (eq. (7)) for each of the three velocity fields of Section 2.

4. An operator-based method: efficient matrix-free algorithm for computing coherent sets

We now focus on the computation of coherent sets using operator based methods as developed by Froyland et. al. [30, 59, 34] on realistic velocity data. An issue to address is the large computational cost of assembling matrices associated with functional operators and of computing their spectral decomposition. The main contribution of this section is to propose a simple and efficient matrix-free method that computes coherent sets based on an Eulerian or Lagrangian flow-map representation [38, 60, 61] at the same spatial resolution as the numerical flow (number of trajectories mimics the resolution of the spatial discretization).

The interpretation of coherent sets as subdomains of smooth functions in the language of Sobolev space, the use of power iterations to compute them, and the exploitation of the zero diffusion-limit in our algorithm are the main originality of this section. However, our numerical method (presented in Algorithm 1 below) relies on several aspects of the theory of coherent sets that are briefly reviewed throughout the section.

Consequently, we provide in Section 4.1 a short review of the transfer operator method interpreted in a

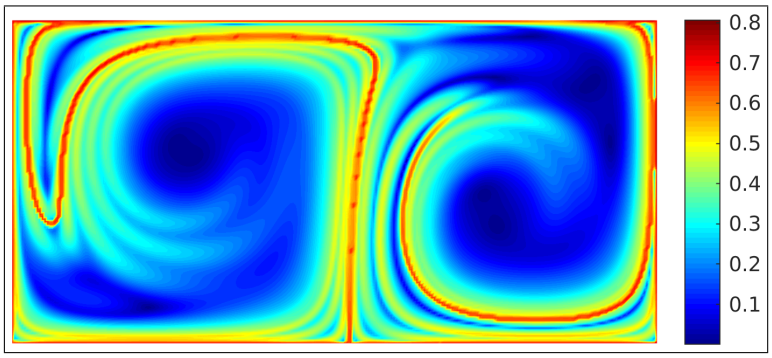

(a) Forward FTLE field of the Double Gyre Flow of Section 2.1(forward time, from $t = 0$ to $t = 15$)

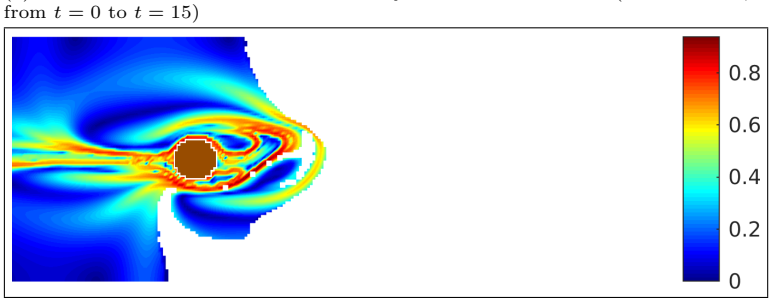

(b) Forward FTLE field of the Flow Past a Cylinder of Section 2.2 (forward time, from $t = 0$ to $t = 10$).

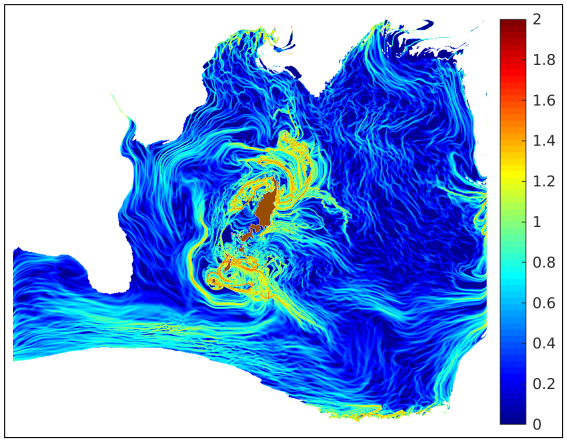

(c) Forward FTLE field of the Palau Island flow of Section 2.3 from May 8th 2015 (forward time, from $t = 0$ to $t = 6$ days), in day^{-1} (color scale).

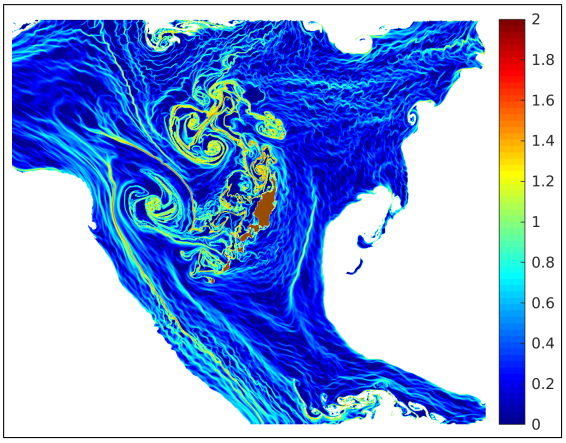

(d) Backward FTLE field of the Palau Island flow of Section 2.3 from May 14th 2015 (backward time, from $t = 6$ days to $t = 0$), in day^{-1} (color scale).

Figure 5: Plots of the FTLE field $\mathrm{FTLE}_0^t(\boldsymbol{x})$ (eq. (5)) for the each of the three velocity fields of Section 2. The white area corresponds to locations of particles that either leave rectangular domain (forward time) or that have not been reached (backward time).

Sobolev space framework (following [34]) rather than in the more classical language of ergodic theory (as e.g. in [30]). Our matrix-free algorithm is then introduced in Section 4.2; its efficiency takes advantage of the power method and of the zero diffusion limit relating the Singular Value Decomposition of the transfer operator to that of the dynamic Laplacian. Finally, we present our numerical results for the three previous benchmark flow examples in Section 4.3, so as to offer the comparison with diffeomorphism based methods.

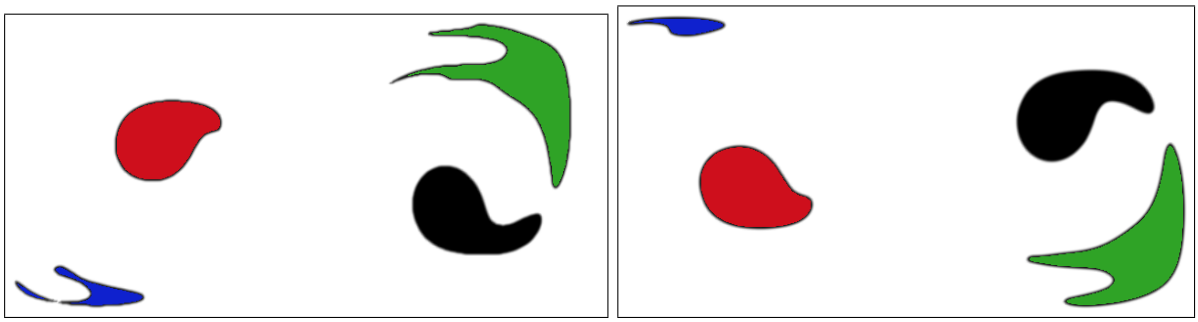

(a) Double Gyre Flow of Section 2.1 (*left*: $t = 0$, and *right*: $t = 15$)

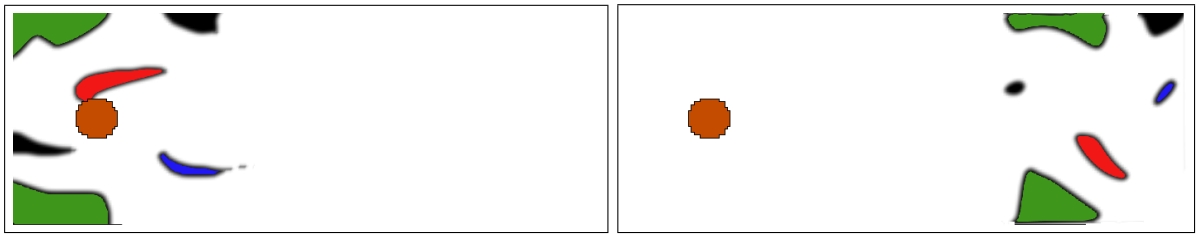

(b) Flow Past a Cylinder of Section 2.2 (*left*: $t = 0$, and *right*: $t = 10$)

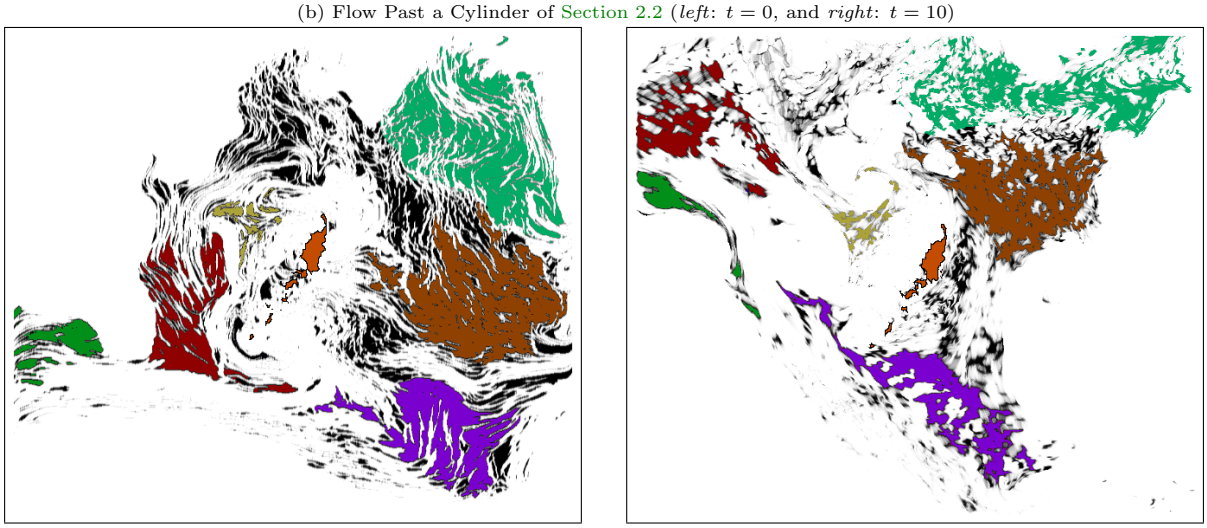

(c) Palau Island flow of Section 2.3 for May 8th - May 14th 2015 (*left*: $t = 0$ days, and *right*: $t = 6$ days)

Figure 6: Initial and final configurations of rigid and approximately rigid sets. Colors have been added to help the reader identify corresponding pairs of rigid sets.

4.1. Definition and properties of coherent sets as zero level-sets of eigenfunctions of a dynamic Laplace operator

Several pioneering works of Froyland et. al. [13, 29, 33, 30, 34] have developed methodologies to decompose the material domain Ω into "coherent partitions", that can be interpreted as a set of subdomains that stir or mix slowly when subjected to material transport by the flow $\boldsymbol{v}(t, x)$. The key idea is to study spectral decompositions of the *push-forward* operator

$$\begin{array}{rccc} \boldsymbol{L} & : & L^2(\Omega, \mathrm{d}\mu(\boldsymbol{x})) & \to & L^2(\boldsymbol{\phi}^t(\Omega), \mathrm{d}\nu(\boldsymbol{y})) \\ & & f & \mapsto & f \circ \boldsymbol{\phi}^{-t}, \end{array} \tag{10}$$

where $L^2(\Omega, \mathrm{d}\mu(\boldsymbol{x}))$ and $L^2(\boldsymbol{\phi}^t(\Omega), \mathrm{d}\nu(\boldsymbol{y}))$ denote the spaces of square integrable functions over the initial and advected domains Ω and $\boldsymbol{\phi}^t(\Omega)$, equipped with respective given measures $\mathrm{d}\mu(\boldsymbol{x})$ and $\mathrm{d}\nu(\boldsymbol{y})$. The operator

$\boldsymbol{L}$ maps a scalar data f labelling all particles at initial positions $\boldsymbol{x} \in \Omega$ with the values $f(\boldsymbol{x})$, to the function $\boldsymbol{L}f = f \circ \boldsymbol{\phi}^{-t}$ obtained by transporting all function values along particles' paths.

Roughly speaking, coherent sets are obtained in the initial and advected configurations from the level-sets of respectively the right and left singular vectors of a regularized version $\boldsymbol{L}_\epsilon \simeq \boldsymbol{L}$ of the transport operator by addition of a small amount of diffusion. In the zero diffusion limit $\epsilon \to 0$, the right eigenvectors converge to the eigenvectors of the Dynamic Laplace operator $\boldsymbol{T} = -\Delta_\Omega - \boldsymbol{L}^* \Delta \boldsymbol{L}$ where $\boldsymbol{L}^*$ is the adjoint of $\boldsymbol{L}$. These results have been first derived by Froyland et. al., by using ideas of ergodic theory [13, 29, 33], and by developing later variational [30, 59] or geometric [34, 31] characterizations. Next, we synthesize these results using the vocabulary of Sobolev's spaces instead of that of ergodic theory.

4.1.1. Coherent sets as minimizers of an energy functional

Based on [34, 31, 36], coherent sets $\mathcal{A}_{coherent}$ are sets that have a "simple geometry" in both the initial and final configurations. As it is classical in functional analysis and shape optimization [62, 63], a class $\mathcal{O}_\rho$ of sets with "simple" geometry can be mathematically defined as the set of negative subdomains of sufficiently smooth functions f, *e.g.* functions of the Sobolev space $H^1(\Omega, \mathrm{d}\mu(\boldsymbol{x}))$ (see [62]) having a Sobolev energy $\int_\Omega |\nabla f|^2 \mathrm{d}\mu(\boldsymbol{x})$ lower than some constant ρ for a given "mass" $\int_\Omega |f|^2 \mathrm{d}\mu(\boldsymbol{x}) = 1$:

$$\mathcal{O}_\rho = \left\{ f^{-1}((-\infty, 0]) \,|\, \int_\Omega |\nabla f|^2 \mathrm{d}\mu(\boldsymbol{x}) \leq \rho \text{ and } \int_\Omega |f|^2 \mathrm{d}\mu(\boldsymbol{x}) = 1 \right\}. \tag{11}$$

Intuitively, sets of $\mathcal{O}_\rho$ have a "simple", smooth geometry for small values of ρ, because the associated functions f cannot oscillate two much (this statement can be made precise by the Courant Nodal domain theorem, see Theorem 13 p111 in [62], vol. 3).

Remark 4. It would also be possible to consider the class of "simple" sets that have a small perimeter for a prescribed volume. This class can be in fact related to (11) by using the Federer-Fleming theorem and Cheeger inequalities (see [34]). In numerical practice, (11) is more convenient to manipulate.

In order to obtain coherent sets as the connected components of negative subdomains $f^{-1}((-\infty, 0]))$, we seek functions f satisfying $\int_\Omega |f|^2 \mathrm{d}x = 1$ and with small values of both energies

$$E^0(f) := \int_\Omega |\nabla f|^2 \mathrm{d}\mu(\boldsymbol{x}), \quad E^t(f) := \int_{\boldsymbol{\phi}^t(\Omega)} |\nabla \boldsymbol{L} f|^2 \mathrm{d}\nu(\boldsymbol{y}).$$

Small values of $E^0(f)$ and $E^t(f)$ are indeed expected to imply that both the associated domain $f^{-1}((-\infty, 0]))$ and its transported configuration $\boldsymbol{L}f^{-1}((-\infty, 0]))$ admit a small number of connected component with simple geometries both in the initial and in the advected configurations. Following [34, 31], we see that a natural way to obtain such functions f is to consider the following minimization problem:

$$\min_{\substack{f \in H^1(\Omega, \mathrm{d}\mu(\boldsymbol{x})) \\ \int_\Omega |f|^2 \mathrm{d}\mu(x) = 1}} J(f) := E^0(f) + E^t(f) = \int_\Omega |\nabla f|^2 \mathrm{d}\mu(\boldsymbol{x}) + \int_{\boldsymbol{\phi}^t(\Omega)} |\nabla(\boldsymbol{L}f)|^2 \mathrm{d}\nu(\boldsymbol{y}). \tag{12}$$

Remark 5. In the definition of eq. (12), it is assumed that the advection operator (eq. (10)),

$$\boldsymbol{L} \,:\, H^1(\Omega, \mathrm{d}\mu(\boldsymbol{x})) \mapsto H^1(\boldsymbol{\phi}^t(\Omega), \mathrm{d}\nu(\boldsymbol{y}))\,, \tag{13}$$

maps $H^1(\Omega, \mathrm{d}\mu(\boldsymbol{x}))$ to $H^1(\boldsymbol{\phi}^t(\Omega), \mathrm{d}\nu(\boldsymbol{y}))$, which is the case if the velocity field $\boldsymbol{v}$ is sufficiently smooth on [64, 65, 34], for example a $\mathcal{C}^1$ function. Indeed, in that case the $H^1(\Omega, \mathrm{d}\mu(\boldsymbol{x}))$ regularity is preserved under the composition with the diffeomorphism $\boldsymbol{\phi}^t$.

Obviously, there is a trivial minimizer to (12) which is the constant function $f_0 = \left|\int_\Omega \mathrm{d}\mu(\boldsymbol{x})\right|^{-1/2}$. f_0 is indeed the most regular function of $H^1(\Omega, \mathrm{d}\mu(\boldsymbol{x}))$, but it defines no coherent set because $f_0((-\infty, 0])) = \emptyset$. However (12) is related to an eigenvalue problem which admits solutions on smaller functional spaces.

Proposition 2 (see Froyland (2015) [34])**.** *Consider the bilinear form $a(f,g)$ defined by*

$$\forall f,g \in H^1(\Omega, \mathrm{d}\mu(\boldsymbol{x})), \quad a(f,g) = \int_\Omega \nabla f \cdot \nabla g \mathrm{d}\mu(\boldsymbol{x}) + \int_{\boldsymbol{\phi}^t(\Omega)} \nabla(\boldsymbol{L}f) \cdot \nabla(\boldsymbol{L}g) \mathrm{d}\nu(\boldsymbol{y}), \tag{14}$$

where the dot $\cdot$ denotes the usual scalar product over 2D or 3D vectors. There exists an orthonormal basis of eigenfunctions $(f_k)_{k\in\mathbb{N}}$ of $L^2(\Omega, \mathrm{d}\mu(\boldsymbol{x}))$ and a diverging and increasing sequence of associated positive eigenvalues $(\lambda_k)_{k\in\mathbb{N}}$ satisfying,

$$f_k \in H^1(\Omega, \mathrm{d}\mu(\boldsymbol{x})) \text{ and } \forall g \in H^1(\Omega, \mathrm{d}\mu(\boldsymbol{x})),\ a(f_k, g) = \lambda_k \int_\Omega f_k g \mathrm{d}\mu(\boldsymbol{x})\,. \tag{15}$$

The first eigenvalue is $\lambda_0 = J(f_0) = 0$ and its associated eigenvector is the constant function $f_0 = (\int_\Omega \mathrm{d}\mu(x))^{-1/2}$. These functions (f_k) are the solution of the minimization problem (12) in the following sense:

- *The constant function f_0 is the solution to the minimization problem (12) with cost value $\lambda_0 = 0$.*
- *If $k > 0$, f_k is a solution of the minimization problem:*

$$\lambda_k = J(f_k) = \min_{\substack{f\in H^1(\Omega,\mathrm{d}\mu(\boldsymbol{x})) \\ \int_\Omega |f|^2 \mathrm{d}x = 1 \\ f \in \mathrm{span}(f_i)_{0\le i\le k-1}^\perp}} J(f) = \int_\Omega |\nabla f|^2 \mathrm{d}\mu(\boldsymbol{x}) + \int_{\boldsymbol{\phi}^t(\Omega)} |\nabla(\boldsymbol{L}f)|^2 \mathrm{d}\nu(\boldsymbol{y}). \tag{16}$$

  where the minimization includes the additional constraint that f_k is orthogonal to the space orthogonal to the first k eigenvectors $f_0, \ldots, f_{k-1}$.

Proposition 2 yields functions f satisfying $\int_\Omega |f|^2 \mathrm{d}\mu(\boldsymbol{x}) = 1$ with an energy $J(f) \le \lambda_k$, by considering functions $f \in \mathrm{span}(f_i)_{1\le i\le k}$ in the space spanned by the first k eigenfunctions. Since the first eigenvalue λ_0 is null and associated with the space of constant functions, higher order eigenvectors satisfy the orthogonality condition $\int_\Omega f_k \mathrm{d}\mu(\boldsymbol{x}) = 0$ for $k \ge 2$. This implies that an identical amount of mass is distributed in either component of the zero level-set function, which suggests that the zero level-set may be an adequate candidate for delimiting coherent sets, which is the strategy retained in this paper. In [30], such level set was rather selected by solving an additional minimization problem. This synthesis also makes clear that the computation of eigenfunctions of order k greater than 2 is advantageous.

Definition 3. Given a choice of measures $\mu(x)$ and $\nu(y)$, the coherent sets of order $k \ge 1$ are defined to be the connected components of the partition of Ω induced by the negative subdomains $f_k((-\infty, 0))$ of the eigenvector f_k of (15).

4.1.2. Choice of initial and image measures

In general and in this paper, one sets the initial and the image measures according to,

$$\begin{aligned} \mathrm{d}\mu(\boldsymbol{x}) &= \mathrm{d}\boldsymbol{x} \\ \mathrm{d}\nu(\boldsymbol{y}) &= |\det(\mathrm{D}\boldsymbol{\phi}^t)|^{-1} \circ \boldsymbol{\phi}^{-t}(\boldsymbol{y}) \mathrm{d}\boldsymbol{y}, \end{aligned} \tag{17}$$

where $\mathrm{d}\boldsymbol{x}$ and $\mathrm{d}\boldsymbol{y}$ are the usual Lebesgue measures over the domains Ω and $\boldsymbol{\phi}^t(\Omega)$. This has the advantage of implying the following convenient fact (see [31]):

Proposition 3. *Assuming the choice of measure (17), the operator $\boldsymbol{L}^{-1} : f \mapsto f \circ \boldsymbol{\phi}^t$ is both the inverse of the transport operator $\boldsymbol{L}$ (eq. (10)) and its adjoint with respect to the scalar products of $L^2(\Omega, \mathrm{d}\mu(\boldsymbol{x}))$ and $L^2(\boldsymbol{\phi}^t(\Omega), \mathrm{d}\nu(\boldsymbol{y}))$, namely $\boldsymbol{L}^* = \boldsymbol{L}^{-1}$ and the following identity holds:*

$$\forall f \in H^1(\Omega, \mathrm{d}\mu(\boldsymbol{x})), g \in H^1(\boldsymbol{\phi}^t(\Omega), \mathrm{d}\nu(\boldsymbol{y})),\ \int_{\boldsymbol{\phi}^t(\Omega)} (\boldsymbol{L}f)(\boldsymbol{y}) g(\boldsymbol{y}) \mathrm{d}\nu(\boldsymbol{y}) = \int_\Omega f(\boldsymbol{x}) (\boldsymbol{L}^{-1} g)(\boldsymbol{x}) \mathrm{d}\mu(\boldsymbol{x}). \tag{18}$$

In particular, (18) implies that both energies $\int_\Omega |\nabla f|^2 \mathrm{d}\mu(\boldsymbol{x})$ and $\int_{\boldsymbol{\phi}^t(\Omega)} |\nabla(\boldsymbol{L}f)|^2 \mathrm{d}\nu(\boldsymbol{y})$ in the definition (12) are weighted relatively to the same mass constraint $\int_{\boldsymbol{\phi}^t(\Omega)} |\boldsymbol{L}f|^2 \mathrm{d}\nu(\boldsymbol{y}) = \int_\Omega |f|^2 \mathrm{d}\mu(\boldsymbol{x}) = 1$.

If $\boldsymbol{L}$ is volume preserving, *i.e.* if the velocity field is divergent free ($\mathrm{div}(\boldsymbol{v}) = 0$), the image measure $\mathrm{d}\nu(\boldsymbol{y})$ and the initial measure are identically equal to the Lebesgue measure: $\mathrm{d}\mu(\boldsymbol{x}) = \mathrm{d}\boldsymbol{x}$ and $\mathrm{d}\nu(\boldsymbol{y}) = \mathrm{d}\boldsymbol{y}$.

4.1.3. Strong form of the dynamic Laplace operator

The dynamic Laplace operator has been introduced in [34] as follows.

Definition 4. Assuming the choice of measures (17), the dynamic Laplace operator is the operator $\boldsymbol{T} : H^1(\Omega, \mathrm{d}\mu(\boldsymbol{x})) \to H^{-1}(\Omega, \mathrm{d}\mu(\boldsymbol{x}))$ defined by

$$\boldsymbol{T} = -\Delta - \boldsymbol{L}^* \Delta_{\boldsymbol{\phi}^t(\Omega)} \boldsymbol{L}. \tag{19}$$

The following proposition states that the functions f_k are the eigenvectors of $\boldsymbol{T}$ equipped with suitable boundary conditions. We also refer to [31] for further generalizations.

Proposition 4 (see Froyland (2015) [34])**.** *Assuming the choice of measure (17), the sequence (f_k) defined in Proposition 2 are solutions to the following eigenvalue problem:*

$$\begin{cases} -\Delta f_{\Omega,k} - [\Delta(f_k \circ \boldsymbol{\phi}^{-t})] \circ \boldsymbol{\phi}^t = \lambda_k f_k \ \text{in } \Omega \\ \nabla f_k \cdot (I + (\mathrm{D}\boldsymbol{\phi}^{-t})(\mathrm{D}\boldsymbol{\phi}^{-t})^T)\mathbf{n} = 0 \ \text{on } \partial\Omega, \end{cases} \tag{20}$$

where $\boldsymbol{n}$ is the outward normal to $\partial\Omega$ and $-\Delta = -\sum_{i=1}^n \partial_i^2$ is the usual Laplace operator.

4.2. Efficient computation of coherent sets using the zero-diffusion limit and matrix-free evaluations

We now present our matrix-free methodology to compute coherent sets, relying on the characterization (20) rather than on the eigenvalue problem (15) given in variational form. We start by providing a few remarks regarding the issues arising in the computation of the eigenvalues of the dynamic Laplace operator (19) with standard finite element methods. We then present an efficient way to solve (20) by relying on

(i) a matrix-free approach for the computation of eigenvectors of the dynamic Laplace operator (19);

(ii) the zero-diffusion limit property [34] which relates the eigenvectors f_k of (20) to the singular vectors of the transfer operator $\boldsymbol{L}$ (10). This allows computing eigenvectors of (20) associated with the smallest eigenvalues.

These two ingredients are detailed next. The whole procedure is summarized in Algorithm 1 below.

4.2.1. Lack of sparsity when using standard finite element eigenvalue solvers

A challenge that arises when trying to solve the eigenvalue problem (15) with the finite element method is the computation of the matrix associated with the bilinear form a of (14) (or in other words, of the discretization of the dynamic Laplace operator $-\Delta_\Omega - \boldsymbol{L}^* \Delta_{\boldsymbol{\phi}^t(\Omega)} \boldsymbol{L}$). Finite-element methods as well as collocations methods have been considered by Froyland in [66].

Generally, the domain Ω is discretized into p mesh elements $\Omega = \cup_{i=1}^p \Omega_i$ with centers $(x_i)_{1 \le i \le p}$ and one considers a standard $\mathbb{P}_1$ Lagrange finite element discretization of the space $H^1(\Omega, \mathbb{R}^n)$ with basis functions $\psi_1, \ldots, \psi_p$) (see e.g. [67]). The matrices $A_{kl} = a(\psi_k, \psi_l)$ and $B_{kl} = \int_\Omega \psi_k \psi_l \mathrm{d}\mu(\boldsymbol{x})$ are then computed and the generalized eigenvalue problem

$$A\boldsymbol{x} = \lambda B \boldsymbol{x} \tag{21}$$

is solved numerically to obtain finite dimensional approximations of the functions f_k satisfying (15).

The matrix A is given by $A = A^1 + A^2$, where A^1 is defined by $A^1_{kl} = \int_\Omega \nabla\psi_k \nabla\psi_l \mathrm{d}\mu(\boldsymbol{x})$ and A^2 is $A^2_{kl} = \int_{\boldsymbol{\phi}^t(\Omega)} \nabla(\boldsymbol{L}\psi_k)\nabla(\boldsymbol{L}\psi_l)\mathrm{d}\nu(\boldsymbol{y})$. The matrix A^1 is sparse, however this is in general not the case for the

matrix A^2 due to numerical diffusion and the exponential stretching of each of the elements $\boldsymbol{\phi}^t(\Omega_i)$. This is mostly visible from the following identity (see e.g. [63]):

$$A^2_{kl} = \int_{\boldsymbol{\phi}^t(\Omega)} \nabla(\boldsymbol{L}\psi_k)\cdot(\nabla \boldsymbol{L}\psi_l)\mathrm{d}\nu(\boldsymbol{y}) = \int_{\Omega} (\mathrm{D}\boldsymbol{\phi}^t)^{-T}\nabla\psi_k \cdot (\mathrm{D}\boldsymbol{\phi}^t)^{-T}\nabla\psi_l |\det(\mathrm{D}\boldsymbol{\phi}^t)|\mathrm{d}\mu(\boldsymbol{x}).$$

The matrix A^2 is not sparse because the transported gradient $(\mathrm{D}\boldsymbol{\phi}^t)^{-T}\nabla\psi_k$ has in general a support intersecting the one of $(\mathrm{D}\boldsymbol{\phi}^t)^{-T}\nabla\psi_l$. As a consequence, the matrix A^2 tends to be a large dense matrix even for moderate integration times. Hence, solving the eigenvalue problem (21) becomes very expensive as soon as the resolution of the input velocity fields becomes large.

Remark 6. The initial works of Froyland et. al. [30] relied on the Ulam Galerkin method which considers basis functions ψ_k that do not even belong to the space $H^1(\Omega, \mathrm{d}\mu(\boldsymbol{x}))$ (namely $\psi_k = \mathbf{1}_{\Omega_k}$ are the characteristic functions of the elements Ω_k). More recent works [36, 37] have proposed to use finite element bases adapted to $\boldsymbol{\phi}^t(\Omega)$ in order to make the assembly of A and the solution of (21) computationally tractable.

4.2.2. Matrix-free evaluation of the dynamic Laplace operator

Matrix-free eigenvalue solvers rely on variants of the power method, such as Lanczos or Arnoldi iterations [68, 69]. These algorithms use the classical fact that repeated iterations $\boldsymbol{T}^k f$ of the matrix with an initial data f tend to align with the eigenvector associated with the eigenvalues of largest magnitude. Only matrix-vector products $\boldsymbol{T}f$ need to be evaluated, which alleviates the need for computing and storing all the coefficients T_{kl}.

Presently, matrix-vector products $\boldsymbol{T}f$ of the dynamic Laplace operator (19) can be evaluated efficiently, by using e.g. sparse finite dimensional approximations of the Laplace operators $-\Delta_\Omega$ and $\Delta_{\boldsymbol{\phi}^t(\Omega)}$, and efficient matrix-free evaluations of the finite dimensional approximations of advected functions $\boldsymbol{L}f$ and $\boldsymbol{L}^* = \boldsymbol{L}^{-1}g$ with $g = \Delta(\boldsymbol{L}f)$. The latter is possible thanks to an interpolation scheme of $\boldsymbol{L}f$ on the computational domain Ω (known at locations $\boldsymbol{\phi}^t(x_i)$ of the advected grid points $(x_i)_{1\leq i\leq p}$).

4.2.3. The zero-diffusion limit for computing smallest eigenvalues

From Proposition 2, coherent sets of lowest orders k are obtained from of the eigenvectors f_k of the dynamic Laplace operator $\boldsymbol{T}$ associated with the eigenvalues λ_k of *smallest* magnitudes. Consequently, we can not use the power method directly on the operator $\boldsymbol{T}$ (19), which would yield eigenvectors associated with eigenvalues of the *largest* magnitudes. Usually, matrix-free iterative algorithms compute power iterations of the inverse $\boldsymbol{T}^{-1}$ in order to find the smallest eigenvalues of $\boldsymbol{T}$. Additional matrix-free iterative algorithms can for instance be used to solve for such linear inversion (with e.g., conjugate gradient methods [68]).

In this paper, we rely on the advantageous use of the zero-diffusion limit highlighted by Froyland in [34] in order to avoid such inversion.

Theorem 3 (Froyland (2015) [34])**.** *For any $\epsilon > 0$, consider the operator $\boldsymbol{T}_\epsilon$ defined by*

$$\begin{array}{rccl} \boldsymbol{T}_\epsilon & : & H^1(\Omega,\mathrm{d}\mu(\boldsymbol{x})) & \longrightarrow & H^{-1}(\Omega,\mathrm{d}\mu(\boldsymbol{x})) \\ & & f & \longmapsto & \dfrac{I-(I-\epsilon\Delta_\Omega)^{-\frac{1}{2}}\boldsymbol{L}^*(I-\epsilon\Delta_{\boldsymbol{\phi}^t(\Omega)})^{-1}\boldsymbol{L}(I-\epsilon\Delta_\Omega)^{-\frac{1}{2}}}{\epsilon} f. \end{array}$$

Then, $\boldsymbol{T}_\epsilon f \rightharpoonup \boldsymbol{T}f$ weakly-$*$ in $H^{-1}(\Omega,\mathrm{d}\mu(\boldsymbol{x}))$.

Remark 7. The weak-$*$ convergence $\boldsymbol{T}_\epsilon \rightharpoonup \boldsymbol{T}$ means that for any functions $f, g \in H^1(\Omega,\mathrm{d}\mu(\boldsymbol{x}))$, it holds $\langle \boldsymbol{T}_\epsilon f, g\rangle \to \langle \boldsymbol{T}f, g\rangle$ where $\langle\cdot,\cdot\rangle$ is the duality product between $H^{-1}(\Omega,\mathrm{d}\mu(\boldsymbol{x}))$ and $H^1(\Omega,\mathrm{d}\mu(\boldsymbol{x}))$.

Remark 8. The regularization operator $(I-\epsilon\Delta_\Omega)^{-\frac{1}{2}} : L^2(\Omega,\mathrm{d}\mu(\boldsymbol{x})) \to H^1(\Omega,\mathrm{d}\mu(\boldsymbol{x}))$ is defined from any standard definition of fractional power [70], e.g.

$$\begin{array}{rccl} (I-\epsilon\Delta_\Omega)^{-\frac{1}{2}} & : & L^2(\Omega,\mathrm{d}\mu(\boldsymbol{x})) & \to & H^1(\Omega,\mathrm{d}\mu(\boldsymbol{x})) \\ & & f & \longmapsto & \sum_{k\in\mathbb{N}} \frac{1}{(1+\epsilon\mu_k)^{1/2}}\langle e_k, f\rangle_{L^2(\Omega)} e_k. \end{array} \tag{22}$$

where $(\mu_k)_{k\in\mathbb{N}}$ and $(e_k)_{k\in\mathbb{N}}$ are the eigenvalues and an orthonormal basis of eigenvectors of $-\Delta_\Omega$ with Neumann boundary conditions, respectively. The operator $(I-\epsilon\Delta_{\boldsymbol{\phi}^t(\Omega)})^{-\frac{1}{2}}$ on $L^2(\boldsymbol{\phi}^t(\Omega),\mathrm{d}\nu(\boldsymbol{y}))$ can be defined in a similar manner.

Theorem 3 suggests therefore that the eigenvectors (f_k) of $-\Delta_\Omega - \boldsymbol{L}^*\Delta_{\boldsymbol{\phi}^t(\Omega)}\boldsymbol{L}$ can be approximated by eigenvectors of $\boldsymbol{L}_\epsilon^*\boldsymbol{L}_\epsilon$ where $\boldsymbol{L}_\epsilon$ is the "diffusive" approximation

$$\boldsymbol{L}_\epsilon = (I-\epsilon\Delta_{\boldsymbol{\phi}^t(\Omega)})^{-\frac{1}{2}}\boldsymbol{L}(I-\epsilon\Delta_\Omega)^{-\frac{1}{2}} \simeq \boldsymbol{L}. \tag{23}$$

Remark 9. The coefficient ϵ in (22) quantifies the intensity of the regularization induced by the smoothing operators $(I-\epsilon\Delta_\Omega)^{-\frac{1}{2}}$ and $(I-\epsilon\Delta_{\boldsymbol{\phi}^t(\Omega)})^{-1}$. It must be chosen both sufficiently small so as to ensure that the approximation (23) holds, and sufficiently large so as to allow eigenvalues of $\boldsymbol{L}_\epsilon^*\boldsymbol{L}_\epsilon$ (which all converge to 1 as $\epsilon\to 0$ since $\boldsymbol{L}_\epsilon^*\boldsymbol{L}_\epsilon$ converges to the identity) to be distinguished by numerical algorithms. $\boldsymbol{L}_\epsilon$ can be interpreted as a diffusive transport operator that accounts for the introduction of a small quantity of artificial/numerical diffusion in the purely advective dynamics (2), or of a small random noise in the deterministic particle trajectories (1) (see also the discussions in [71]).

Remark 10. The original statement of Theorem 3 in [34] states that the convergence $\boldsymbol{T}_\epsilon \rightharpoonup T$ still holds (up to a multiplicative constant) when the smoothing operators $(I-\epsilon\Delta_\Omega)^{-\frac{1}{2}}$ and $(I-\epsilon\Delta_{\boldsymbol{\phi}^t(\Omega)})$ are replaced with any isotropic regularizing kernels. This implies the important property that the right singular vectors $f_{k,\epsilon}$ of $\boldsymbol{L}_\epsilon$ (eq. (23)) *become independent of the nature of the added diffusion when* $\epsilon\to 0$. This has the notable benefit of yielding a computational methodology that is "robust to the numerical advection schemes", in the sense that singular vectors $f_{k,\epsilon}$ of $\boldsymbol{L}_\epsilon$ are thus moderately insensitive to the (unknown) numerical diffusion affecting any discrete approximation of the advected functions $\boldsymbol{L}f$.

Remark 11. Computing coherent sets from the Singular Value Decomposition of $\boldsymbol{L}_\epsilon$ rather than from the spectral decomposition of the dynamic Laplace operator $\boldsymbol{T}$ was the original framework proposed by Froyland [30]. Physically, right singular vectors $f_{\epsilon,k}$ of $\boldsymbol{L}_\epsilon$ are the most "resistant" functions to diffusion when advected by the flow. Indeed, singular values $\sigma_{k,\epsilon}\simeq(1-\epsilon\lambda_k)^{1/2}$ of the operator $\boldsymbol{L}_\epsilon$ with corresponding right and left singular vectors $f_{k,\epsilon}$, $g_{k,\epsilon}=\boldsymbol{L}_\epsilon f_{k,\epsilon}$ solve the following maximization problem:

$$\sigma_{k,\epsilon} = \langle \boldsymbol{L}_\epsilon f_{k,\epsilon}, g_{k,\epsilon}\rangle_{L^2(\Omega,\mathrm{d}\mu(\boldsymbol{x}))} = \max_{\substack{f\in H^1(\Omega,\mathrm{d}\mu(\boldsymbol{x})),\\ g\in H^1(\boldsymbol{\phi}^t(\Omega),\mathrm{d}\nu(\boldsymbol{y})),\\ \int_\Omega |f|^2\mathrm{d}\mu(\boldsymbol{x})=\int_{\boldsymbol{\phi}^t(\Omega)}|g|^2\mathrm{d}\nu(\boldsymbol{y})=1\\ g\in\mathrm{span}(g_j)_{j<i}^\perp, f\in\mathrm{span}(f_j)_{j<i}^\perp}} \langle \boldsymbol{L}_\epsilon f, g\rangle_{L^2(\Omega,\mathrm{d}\mu(\boldsymbol{x}))}. \tag{24}$$

Under pure advection, and with the choice of measure (17), the mass of a function f is conserved in the sense that $\int_\Omega |f|^2\mathrm{d}\mu(\boldsymbol{x}) = \int_{\boldsymbol{\phi}^t(\Omega)}|\boldsymbol{L}f|^2\mathrm{d}\nu(\boldsymbol{y})$. If a small amount of diffusion ϵ is added in such a way that $\boldsymbol{L}$ is replaced with $\boldsymbol{L}_\epsilon$, $\boldsymbol{L}_\epsilon f$ suffers from a loss of mass: $\int_{\boldsymbol{\phi}^t(\Omega)}|\boldsymbol{L}_\epsilon f|^2\mathrm{d}\nu(\boldsymbol{y}) < \int_\Omega |f|^2\mathrm{d}\mu(\boldsymbol{x})$. From (24), functions belonging to the subspace $\mathrm{span}(f_{i,\epsilon})_{i\le k}$ will be affected by a loss of mass by a factor at most $\sigma_{k,\epsilon}$. Since the singular values $\sigma_{k,\epsilon}$ are close to 1 for the first values of k, $\mathrm{span}(f_{i,\epsilon})_{i\le k}$ can be understood as the k dimensional subspace of initial data that is *the most resistant to diffusion*.

The key advantage offered by the operator $\boldsymbol{L}_\epsilon$ lies in the fact that the largest singular values of the compact, Hilbert-Schmidt operator $\boldsymbol{L}_\epsilon$ correspond to the *smallest* eigenvalues of the dynamic Laplace operator $\boldsymbol{T}$. Furthermore, matrix-vector products $\boldsymbol{L}_\epsilon f$ can still be evaluated without the need for storing a discretization matrix of $\boldsymbol{L}_\epsilon$. This enables computing approximate eigenvectors $f_{k,\epsilon}\simeq f_k$ corresponding to these eigenvalues without the need for evaluating the inverse $\boldsymbol{T}^{-1}$.

Our new numerical methodology is summarized in Algorithm 1. In our implementation, the domain Ω is rectangular and is discretized into a finite dimensional grid with nodal points $(x_i,y_j)_{1\le i\le p,1\le j\le q}$ and grid spacing $\Delta x,\Delta y>0$. We use trajectory integration of the ODE (1) for the computation of the flow map $\boldsymbol{\phi}^t$ and its inverse $\boldsymbol{\phi}^{-t}$. Given a discretized scalar function $(f(x_i,y_j))_{1_1\le p,1\le j\le q}$, the vector products $\boldsymbol{L}f$ and $\boldsymbol{L}^*f$ are computed by projecting $f\circ\boldsymbol{\phi}^t$ and $f\circ\boldsymbol{\phi}^{-t}$ on the grid points thanks to a linear interpolation scheme.

Algorithm 1 Matrix-free method for coherent sets extraction

1: Compute a numerical approximation of the flow map $\boldsymbol{\phi}^t$ and of its inverse $\boldsymbol{\phi}^{-t}$, using e.g., trajectory integration of each of the grid points or an eulerian method [38, 60, 61].

2: Assuming the choice of measures (17) and for any finite-dimensional approximation of a function f, matrix-free estimations of $\boldsymbol{L}f = f \circ \boldsymbol{\phi}^{-t}$ and $\boldsymbol{L}^* f = f \circ \boldsymbol{\phi}^t$ are computed by using direct interpolation of f at advected points $\boldsymbol{\phi}^t(x_i, y_j)$ or $\boldsymbol{\phi}^{-t}(x_i, y_j)$ (using e.g., `interpn` in MATLAB)

3: A diffusive approximation $\boldsymbol{L}_\epsilon$ of $\boldsymbol{L}$ is estimated by composition with self-adjoint regularizing operators $j_{\Omega,\epsilon}$ and $j_{\boldsymbol{\phi}^t(\Omega),\epsilon}$ as in [59]:

$$\boldsymbol{L}_\epsilon = j_{\boldsymbol{\phi}^t(\Omega),\epsilon} \boldsymbol{L} j_{\Omega,\epsilon},\ \boldsymbol{L}_\epsilon^* = j_{\Omega,\epsilon} \boldsymbol{L}^* j_{\boldsymbol{\phi}^t(\Omega,\epsilon)}. \tag{25}$$

In (23), one has $j_{\Omega,\epsilon} = (I - \epsilon\Delta_\Omega)^{-\frac{1}{2}}$ and $j_{\boldsymbol{\phi}^t(\Omega,\epsilon)} = (I - \epsilon\Delta_{\boldsymbol{\phi}^t(\Omega)})^{-\frac{1}{2}}$. If the diffusion satisfies the CFL condition $\epsilon < (\Delta y^2 + \Delta x^2)/2$, the linear inversion can be avoided by using explicit schemes, e.g.,

$$j_{\Omega,\epsilon}((f_{i,j})_{i,j}) = \left(f_i + \frac{\epsilon}{2} \frac{f_{i+1,j} - 2f_{i,j} + f_{i-1,j}}{\Delta x^2} + \frac{\epsilon}{2} \frac{f_{i,j+1} - 2f_{i,j} + f_{i,j-1}}{\Delta y^2} \right)_{i,j},$$

for central finite-differences at internal nodes, where $(f_{i,j})_{i,j} \equiv (f(x_i, y_j))_{i,j}$ is the discretization of a function f. Alternatively, a power of such operator or more general shapiro filters [74, 72, 60]) can be used if larger values of the diffusion ϵ are needed.

4: Finally, estimate dominant eigenvectors of $\boldsymbol{L}_\epsilon^* \boldsymbol{L}_\epsilon$ by using any iterative method that evaluates only matrix-vector products such as Lanczos or Arnoldi iterations (see e.g. [68]). Our implementation relies on the MATLAB function `eigs` with the functional operator $\boldsymbol{L}_\epsilon$ as an argument (instead of a matrix).

Finally, the operators $(I - \epsilon\Delta_\Omega)^{-\frac{1}{2}}$ and $(I - \epsilon\Delta_{\boldsymbol{\phi}^t(\Omega)})^{-\frac{1}{2}}$ are approximated by using finite differences. In our own numerical application, we found advantageous to increase the amount of diffusion by replacing these operators with the third power $j_\epsilon(f_i) = (\mathcal{F}^{(1)})^3$ of a first order Shapiro filter $\mathcal{F}^{(1)}$ (see [72, 73, 20]).

Remark 12. An alternative approach to Algorithm 1 suggests to estimate singular vectors f_k from a low rank estimation of the operator $\boldsymbol{L}_\epsilon$, which could be used in the case where computing many Arnoldi iterations would become too expensive. These results are detailed and illustrated in [20].

4.3. Numerical results

The numerical methodology of Algorithm 1 is now illustrated on the three benchmark flow examples introduced in Section 2.

For comparison with prior results, we first include in our study the double gyre test case considered in [59]: the flow velocity $\boldsymbol{v}(t, x)$ is defined by (3) with $A = 0.25$, $\sigma = 0.25$ and $\omega = 2\pi$, and the flow is integrated from $t = 0$ to $t = 2$ on a 256x128 grid. The resulting first 8 singular vectors of the diffusive transfer operator $\boldsymbol{L}_\epsilon$ are shown on Figure 7. This enables one to verify that the second pair of singular vectors computed with Algorithm 1 matches the results of [59] obtained with the Ulam Galerkin method.

Results for the three benchmark flow examples of Section 2 are then shown on Figure 8, Figure 9, and Figure 10, respectively. Note that *right* singular vectors $f_{k,\epsilon}$, which correspond to the *initial* configuration, have been plotted on the *left* while *left* singular vectors $g_{k,\epsilon} = \boldsymbol{L}_\epsilon f_{k,\epsilon}$ have been plotted on the right. Coherent partitions are extracted from the zero level-sets of these eigenvectors, the color scale being set such that red and blue correspond to positive and negative values respectively.

We note the ability of the method to deal with (i) flows having outlets and inlets, by putting all the "mass" of the eigenvectors in areas where the flow remains in the domain, (ii) complex multiscale and multi-dynamics ocean flows that involve potentially high-dimensional and highly resolved velocity fields. The number of connected components of the zero level-set increases with the order k of the singular vector $f_{k,\epsilon}$, yielding coherent sets with more complex geometries. It is interesting to compare these figures to those of Figure 6 and to observe the influence of high forward or backward FTLE values on the shape of the coherent sets in, respectively, the initial or final configuration.

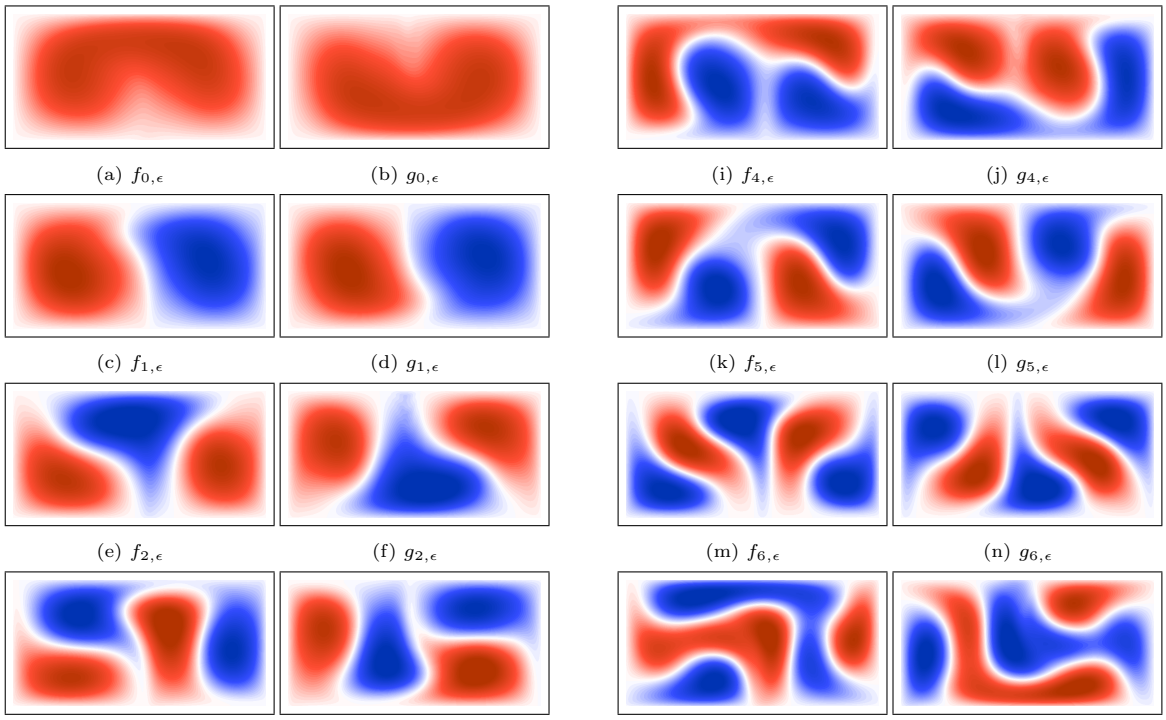

(a) $f_{0,\epsilon}$ (b) $g_{0,\epsilon}$ (i) $f_{4,\epsilon}$ (j) $g_{4,\epsilon}$

(c) $f_{1,\epsilon}$ (d) $g_{1,\epsilon}$ (k) $f_{5,\epsilon}$ (l) $g_{5,\epsilon}$

(e) $f_{2,\epsilon}$ (f) $g_{2,\epsilon}$ (m) $f_{6,\epsilon}$ (n) $g_{6,\epsilon}$

(g) $f_{3,\epsilon}$ (h) $g_{3,\epsilon}$ (o) $f_{7,\epsilon}$ (p) $g_{7,\epsilon}$

Figure 7: Pairs of the first 8 right and left singular vectors $(f_{k,\epsilon})_{0\leq k\leq 7}$ and $(g_{k,\epsilon})_{0\leq k\leq 7}$ of the diffusive operator $\boldsymbol{L}_\epsilon$ for the Double Gyre Flow example of [59] (corresponding to the flow defined by (3) with $A = 0.25$, $\sigma = 0.25$, $\omega = 2\pi$ on the time window $t \in [0, 2]$).

On Figure 8, we plot the first 8 pairs of singular vectors for the Double Gyre Flow of Section 2.1. Due to the symmetrical role played by the two vortices, we obtain similar coherent sets as the blue and red regions in the left and right half portion of the domain, respectively. Similarity are found with the rigid shapes found in Figure 6a, for instance the red and blue regions of $f_{2,\epsilon}$ and $f_{3,\epsilon}$. However, further coherent partitions are found on the remaining singular vectors.

On Figure 9, we plot a set of 4 pairs of singular vectors for the Flow Past a Cylinder of Section 2.2. We chose the singular vectors of order 2, 3, 5 and 12 so as to show that relevant coherent partitions may be found in higher order singular vectors. Interestingly, five small coherent sets are identified as the blue regions on Figure 9(g), which are approximately superimposed on the rigid sets depicted on Figure 6b. Similarly, these plots illustrate how the material transport of particles to the right is affected by the mixing due to the oscillations of the flow in the direction transverse to the pipe.

Finally, coherent sets are computed for the high-dimensional Palau Island flow of Section 2.3. We display on Figure 10 a selection of five coherent partitions. For this example, the gap between the first singular values is small and the resulting coherent partitions seem of similar relevance. Again, we find similarities between the boundaries of some of the coherent sets and the rigid sets identified on Figure 6c, for instance the left red set of $f_{7,\epsilon}$ matches approximatively the left green rigid set of Figure 6c. However singular vectors of higher order enable to extract other possible determinations of coherent partitions.

Our results highlight that the coherent sets identified with the operator based method differ logically from the rigid sets obtained from the thresholding of the polar distance in eq. (8): coherent sets divide the domain into regions that "mix" one another slowly, large stretching are allowed within their boundaries. We note that due to the smoothing nature of the eigenvalue problem, the first pairs of coherent sets are very smooth and gradually become more complex as their rank k of the associated eigenvector f_k increases. In contrast with rigid sets which are less smooth, coherent stes are therefore able to distinguish a hierachy of scales in material transport, which is most visible in the Palau example featuring multiscale ocean currents fields. Depending on what definition of coherence is sought, this enables to extract non-mixing material

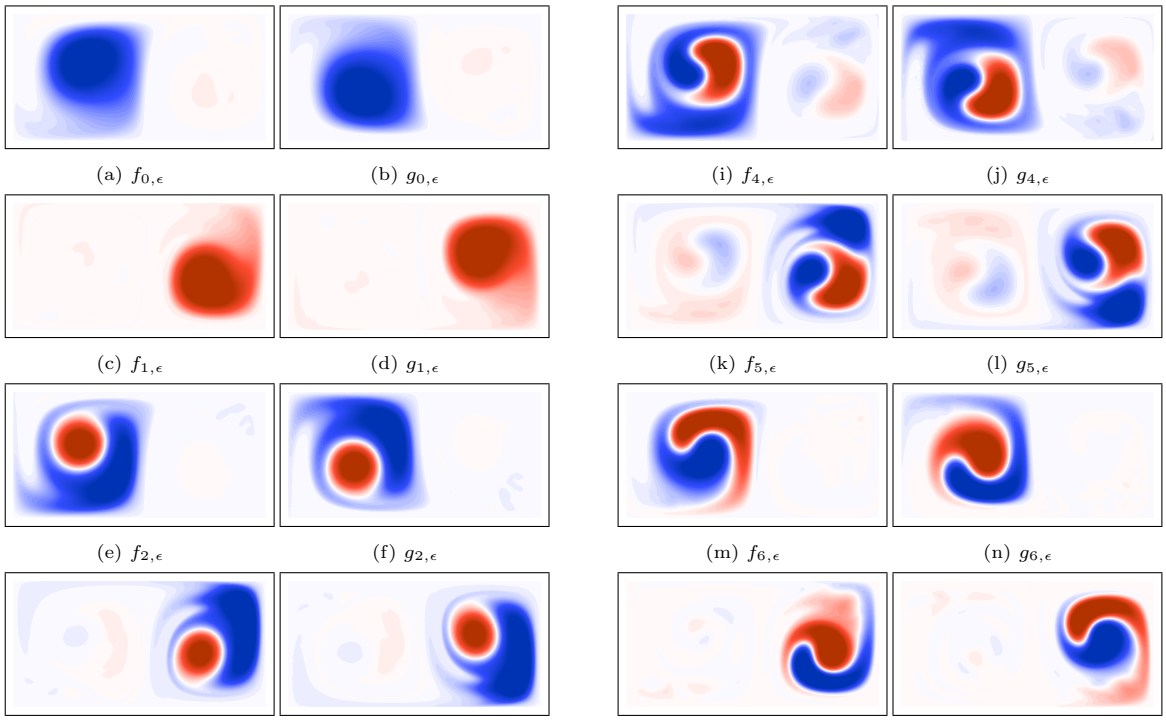

(a) $f_{0,\epsilon}$ (b) $g_{0,\epsilon}$ (i) $f_{4,\epsilon}$ (j) $g_{4,\epsilon}$
(c) $f_{1,\epsilon}$ (d) $g_{1,\epsilon}$ (k) $f_{5,\epsilon}$ (l) $g_{5,\epsilon}$
(e) $f_{2,\epsilon}$ (f) $g_{2,\epsilon}$ (m) $f_{6,\epsilon}$ (n) $g_{6,\epsilon}$
(g) $f_{3,\epsilon}$ (h) $g_{3,\epsilon}$ (o) $f_{7,\epsilon}$ (p) $g_{7,\epsilon}$

Figure 8: Pairs of corresponding right and left singular vectors $f_{k,\epsilon}$ and $g_{k,\epsilon}$ for $k = 0$ to $k = 7$ of the diffusive operator $\boldsymbol{L}_\epsilon$ for the Double Gyre Flow of Section 2.1 (eq. (3) with $A = 0.1$, $\sigma = 0.1$ and $\omega = 2\pi/10$ on the time window $t \in [0, 15]$).

regions even if intense stretching occurs uniformly in the working domain (in such a case, diffeomorphism based methods presented in Section 3 would not detect any rigid set). The picture of Lagrangian transport that is obtained from this operator method is therefore complementary to the one obtained from the one based on the polar distance.

5. Conclusion

Two methodologies have been developed and applied so as to extract two kinds of Lagrangian coherent subdomains from realistic complex velocity fields characterized by inlets and outlets, potentially highly resolved grids, and non necessarily divergence-free flows. A new criterion was proposed to define and extract *rigid sets* efficiently in the context of *diffeomorphism-based* methods. The theory of *coherent sets* developed by Froyland et. al. [30, 34] based on *operator methods* was reviewed and synthesized. A new efficient matrix-free algorithms exploiting the zero diffusion limit was proposed for the computation of coherent sets. Both approaches were illustrated and compared on three sets of benchmark numerical flow simulation data, including a high-dimensional, realistic and data-driven simulation of a submesoscale to large-scale ocean current field in the Palau Island region of the western Pacific Ocean.

Our results highlight that rigid sets and coherent sets provide two complementary pictures of material transport in dynamic flow fields. Rigid sets are sets which are transported by the flow almost in a rigid manner between two instants; distances among particles are approximately preserved. Coherent sets determine smooth partitions of the domain in which large mixing is possible, but each partition remains independent of the other. These properties were illustrated on the three different flow fields.

Future works include utilizing methods that efficiently transfer the uncertainty of the flow fields to the LCS and the rigid and coherent sets [75, 76, 77, 78], leading to probabilistic rigid and coherent sets. Extracting the three-dimensional in space rigid and coherent sets [79] would also be useful in realistic ocean and atmospheric applications [80, 81, 82]. The use of tight control on the numerical diffusion using flow

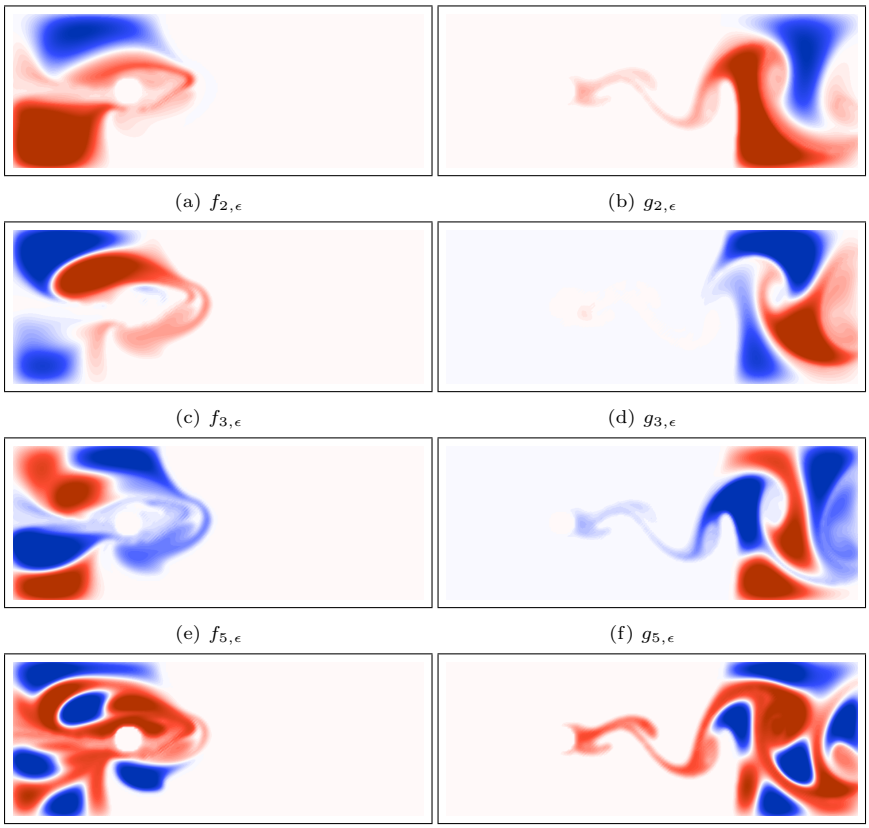

(a) $f_{2,\epsilon}$ (b) $g_{2,\epsilon}$

(c) $f_{3,\epsilon}$ (d) $g_{3,\epsilon}$

(e) $f_{5,\epsilon}$ (f) $g_{5,\epsilon}$

(g) $f_{12,\epsilon}$ (h) $g_{12,\epsilon}$

Figure 9: Approximate right and left singular vectors $f_{k,\epsilon}$ and $g_{k,\epsilon}$ of orders $k \in \{2, 3, 5, 12\}$ of the diffusive transfer operator $\boldsymbol{L}_\epsilon$ for the Flow Past a Cylinder of Section 2.2.

map composition [61] should also be investigated. Finally, quantitative criteria to characterize coherence, stirring, and mixing in geophysical fluid flows [83, 84, 85] such as those that developed here are likely to provide new understanding for complex ocean and atmospheric transports and dynamics.

Acknowledgments

We thank the members of our MSEAS group for insightful discussions. We are grateful to the Office of Naval Research for support under Grants N00014-14-1-0725 (Bays-DA), N00014-15-1-2626 (DRI-FLEAT), and N00014-19-1-2693 (IN-BDA), and to the National Science Foundation (NSF) for support under grant EAR-1520825 (Hazards SEES – ALPHA), each to the Massachusetts Institute of Technology. We thank our colleagues in the Flow Encountering Abrupt Topography (FLEAT) initiative for their collaboration.

References

[1] G. Haller, G. Yuan, Lagrangian coherent structures and mixing in two-dimensional turbulence, Physica D: Nonlinear Phenomena 147 (3) (2000) 352–370.

[2] M. Farazmand, G. Haller, Computing Lagrangian coherent structures from their variational theory, Chaos 22 (1) (2012) 1–12.

[3] G. Haller, F. J. Beron-Vera, Geodesic theory of transport barriers in two-dimensional flows, Physica D: Nonlinear Phenomena 241 (20) (2012) 1680–1702.

[4] G. Haller, Lagrangian coherent structures, Annual Review of Fluid Mechanics 47 (2015) 137–162.

[5] S. Balasuriya, N. T. Ouellette, I. I. Rypina, Generalized lagrangian coherent structures, Physica D: Nonlinear Phenomena 372 (2018) 31–51.

[6] F. Lekien, C. Coulliette, A. J. Mariano, E. H. Ryan, L. K. Shay, G. Haller, J. Marsden, Pollution release tied to invariant manifolds: A case study for the coast of Florida, Physica D: Nonlinear Phenomena 210 (1) (2005) 1–20.

[7] C. Coulliette, F. Lekien, J. D. Paduan, G. Haller, J. E. Marsden, Optimal pollution mitigation in Monterey Bay based on coastal radar data and nonlinear dynamics, Environmental science & technology 41 (18) (2007) 6562–6572.

[8] P. F. J. Lermusiaux, M. Doshi, C. S. Kulkarni, A. Gupta, P. J. Haley, Jr., C. Mirabito, F. Trotta, S. J. Levang, G. R. Flierl, J. Marshall, T. Peacock, C. Noble, Plastic pollution in the coastal oceans: Characterization and modeling, in: OCEANS 2019 MTS/IEEE SEATTLE, IEEE, Seattle, 2019, pp. 1–10. doi:10.23919/OCEANS40490.2019.8962786.

[9] M. Serra, P. Sathe, I. Rypina, A. Kirincich, S. D. Ross, P. Lermusiaux, A. Allen, T. Peacock, G. Haller, Search and rescue at sea aided by hidden flow structures, Nature Communications 11 (2020) 1–7. doi:10.1038/s41467-020-16281-x.

[10] K. L. Scales, E. L. Hazen, M. G. Jacox, F. Castruccio, S. M. Maxwell, R. L. Lewison, S. J. Bograd, Fisheries bycatch risk to marine megafauna is intensified in lagrangian coherent structures, Proceedings of the National Academy of Sciences 115 (28) (2018) 7362–7367.

[11] M. M. Doshi, C. S. Kulkarni, W. H. Ali, A. Gupta, P. F. J. Lermusiaux, P. Zhan, I. Hoteit, O. Knio, Flow maps and coherent sets for characterizing residence times and connectivity in lagoons and coral reefs: The case of the Red Sea, in: OCEANS 2019 MTS/IEEE SEATTLE, IEEE, Seattle, 2019, pp. 1–8. doi:10.23919/OCEANS40490.2019.8962643.

[12] C. B. Paris, S. A. Murawski, M. J. Olascoaga, A. C. Vaz, I. Berenshtein, P. Miron, F. J. Beron-Vera, Connectivity of the gulf of mexico continental shelf fish populations and implications of simulated oil spills, in: Scenarios and Responses to Future Deep Oil Spills, Springer, 2020, pp. 369–389.

[13] G. Froyland, K. Padberg, M. H. England, A. M. Treguier, Detection of coherent oceanic structures via transfer operators, Physical review letters 98 (22) (2007) 224503.

[14] D. Karrasch, Attracting Lagrangian coherent structures on Riemannian manifolds, Chaos: An Interdisciplinary Journal of Nonlinear Science 25 (8) (2015) 087411.

[15] K. Onu, F. Huhn, G. Haller, An Algorithmic Introduction to Lagrangian Coherent Structures (2014).

[16] T. Peacock, G. Haller, Lagrangian coherent structures: The hidden skeleton of fluid flows, Physics Today 66 (2) (2013) 41–47.

[17] S. C. Shadden, F. Lekien, J. E. Marsden, Definition and properties of Lagrangian coherent structures from finite-time Lyapunov exponents in two-dimensional aperiodic flows, Physica D: Nonlinear Phenomena 212 (3) (2005) 271–304.

[18] W. Tang, P. W. Chan, G. Haller, Accurate extraction of Lagrangian coherent structures over finite domains with application to flight data analysis over Hong Kong International Airport, Chaos: An Interdisciplinary Journal of Nonlinear Science 20 (1) (2010) 017502.

[19] M. R. Allshouse, J.-L. Thiffeault, Detecting coherent structures using braids, Physica D: Nonlinear Phenomena 241 (2) (2012) 95–105.

[20] F. Feppon, Riemannian geometry of matrix manifolds for Lagrangian uncertainty quantification of stochastic fluid flows, Master's thesis, Massachusetts Institute of Technology, Department of Mechanical Engineering, Cambridge, Massachusetts (Feb. 2017).

[21] G. Haller, Lagrangian coherent structures from approximate velocity data, Physics of Fluids (1994-present) 14 (6) (2002) 1851–1861.

[22] G. Haller, D. Karrasch, F. Kogelbauer, Material barriers to diffusive and stochastic transport, Proceedings of the National Academy of Sciences 115 (37) (2018) 9074–9079.

[23] G. Haller, A variational theory of hyperbolic Lagrangian coherent structures, Physica D: Nonlinear Phenomena 240 (7) (2011) 574–598.

[24] G. Haller, A. Hadjighasem, M. Farazmand, F. Huhn, Defining coherent vortices objectively from the vorticity, Journal of Fluid Mechanics 795 (2016) 136–173.

[25] D. Oettinger, D. Blazevski, G. Haller, Global variational approach to elliptic transport barriers in three dimensions, Chaos: An Interdisciplinary Journal of Nonlinear Science 26 (3) (2016) 033114.

[26] M. Serra, G. Haller, Objective Eulerian Coherent Structures, arXiv preprint arXiv:1512.02112 (2015).

[27] A. Hadjighasem, D. Karrasch, H. Teramoto, G. Haller, Spectral-clustering approach to lagrangian vortex detection, Physical Review E 93 (6) (2016) 063107.

[28] A. Hadjighasem, M. Farazmand, D. Blazevski, G. Froyland, G. Haller, A critical comparison of lagrangian methods for coherent structure detection, Chaos: An Interdisciplinary Journal of Nonlinear Science 27 (5) (2017) 053104.

[29] G. Froyland, M. Schwalb, K. Padberg, M. Dellnitz, A transfer operator based numerical investigation of coherent structures in three-dimensional Southern Ocean circulation, ratio 1 (2008) 1.

[30] G. Froyland, An analytic framework for identifying finite-time coherent sets in time-dependent dynamical systems, Physica D: Nonlinear Phenomena 250 (2013) 1–19.

[31] G. Froyland, E. Kwok, A dynamic Laplacian for identifying Lagrangian coherent structures on weighted Riemannian manifolds, arXiv preprint arXiv:1610.01128 (2016).

[32] D. Karrasch, J. Keller, A geometric heat-flow theory of lagrangian coherent structures, Journal of Nonlinear Science 30 (4) (2020) 1849–1888.

[33] G. Froyland, S. Lloyd, N. Santitissadeekorn, Coherent sets for nonautonomous dynamical systems, Physica D: Nonlinear Phenomena 239 (16) (2010) 1527–1541.

[34] G. Froyland, Dynamic isoperimetry and the geometry of Lagrangian coherent structures, Nonlinearity 28 (10) (2015) 3587.

[35] G. Froyland, C. Horenkamp, V. Rossi, E. van Sebille, Studying an Agulhas ring's long-term pathway and decay with finite-time coherent sets, Chaos: An Interdisciplinary Journal of Nonlinear Science 25 (8) (2015) 083119.

[36] G. Froyland, O. Junge, Robust fem-based extraction of finite-time coherent sets using scattered, sparse, and incomplete trajectories, SIAM Journal on Applied Dynamical Systems 17 (2) (2018) 1891–1924.

[37] A. Klünker, C. Schneide, G. Froyland, J. Schumacher, K. Padberg-Gehle, Set-oriented and finite-element study of coherent behavior in rayleigh-bénard convection, in: Proceedings of the Workshop on Dynamics, Optimization and Computation held in honor of the 60th birthday of Michael Dellnitz, Springer, 2020, pp. 86–108.
[38] S. Leung, An Eulerian approach for computing the finite time Lyapunov exponent, Journal of computational physics 230 (9) (2011) 3500–3524.
[39] T. M. S. Johnston, M. C. Schönau, T. Paluszkiewicz, J. A. MacKinnon, B. K. Arbic, P. L. Colin, M. H. Alford, M. Andres, L. Centurioni, H. C. Graber, K. R. Helfrich, V. Hormann, P. F. J. Lermusiaux, R. C. Musgrave, B. S. Powell, B. Qiu, D. L. Rudnick, H. L. Simmons, L. St. Laurent, E. J. Terrill, D. S. Trossman, G. Voet, H. W. Wijesekera, K. L. Zeiden, Flow Encountering Abrupt Topography (FLEAT): A multiscale observational and modeling program to understand how topography affects flows in the western North Pacific, Oceanography 32 (4) (2019) 10–21. doi:10.5670/oceanog.2019.407.
[40] P. J. Haley, Jr., P. F. J. Lermusiaux, Multiscale two-way embedding schemes for free-surface primitive equations in the "Multidisciplinary Simulation, Estimation and Assimilation System", Ocean Dynamics 60 (6) (2010) 1497–1537. doi:10.1007/s10236-010-0349-4.
[41] W. G. Leslie, P. J. Haley, Jr., P. F. J. Lermusiaux, M. P. Ueckermann, O. Logutov, J. Xu, MSEAS Manual, MSEAS Report 06, Department of Mechanical Engineering, Massachusetts Institute of Technology, Cambridge, MA (2010).
URL http://mseas.mit.edu/?p=2237
[42] P. J. Haley, Jr., A. Agarwal, P. F. J. Lermusiaux, Optimizing velocities and transports for complex coastal regions and archipelagos, Ocean Modeling 89 (2015) 1–28. doi:10.1016/j.ocemod.2015.02.005.
[43] T. M. S. Johnston, J. A. MacKinnon, P. L. Colin, P. J. Haley, Jr., P. F. J. Lermusiaux, A. J. Lucas, M. A. Merrifield, S. T. Merrifield, C. Mirabito, J. D. Nash, C. Y. Ou, M. Siegelman, E. J. Terrill, A. F. Waterhouse, Energy and momentum lost to wake eddies and lee waves generated by the North Equatorial Current and tidal flows at Peleliu, Palau, Oceanography 32 (4) (2019) 110–125. doi:10.5670/oceanog.2019.417.
[44] J. Cummings, O. Smedstad, Variational data analysis for the global ocean, in: S. Park, L. Xu (Eds.), Data Assimilation for Atmospheric, Oceanic and Hydrologic Applications, Vol. II, Springer-Verlag, 2013. doi:10.1007/978-3-642-35088-7_13.
[45] G. Egbert, S. Erofeeva, Efficient inverse modeling of barotropic ocean tides, jtech 19 (2) (2002) 183–204.
[46] O. G. Logutov, P. F. J. Lermusiaux, Inverse barotropic tidal estimation for regional ocean applications, Ocean Modelling 25 (1–2) (2008) 17–34. doi:10.1016/j.ocemod.2008.06.004.
URL http://www.sciencedirect.com/science/article/pii/S1463500308000851
[47] R. A. Horn, C. R. Johnson, Matrix Analysis, Cambridge University Press (CUP), 2009.
[48] G. Haller, T. Sapsis, Lagrangian coherent structures and the smallest finite-time Lyapunov exponent, Chaos: An Interdisciplinary Journal of Nonlinear Science 21 (2) (2011) 023115.
[49] M. Farazmand, G. Haller, Attracting and repelling Lagrangian coherent structures from a single computation, Chaos: An Interdisciplinary Journal of Nonlinear Science 23 (2) (2013) 023101.
[50] J. Salençon, Mécanique des milieux continus: Concepts généraux, Vol. 1, Editions Ecole Polytechnique, 2005.
[51] C. G. Small, The statistical theory of shape, Springer Science & Business Media, 2012.
[52] F. John, Rotation and strain, Communications on Pure and Applied Mathematics 14 (3) (1961) 391–413.
[53] Y. G. Reshetnyak, Stability theorems in geometry and analysis, Vol. 304, Springer Science & Business Media, 2013.
[54] C. Truesdell, W. Noll, The non-linear field theories of mechanics, Encyclopedia of Physics 3 (1965) 3.
[55] F. Feppon, P. F. J. Lermusiaux, The extrinsic geometry of dynamical systems tracking nonlinear matrix projections, SIAM Journal on Matrix Analysis and Applications 40 (2) (2019) 814–844. doi:10.1137/18M1192780.
[56] J. Lin, P. Lermusiaux, Minimum-correction second-moment matching: theory, algorithms and applications, Numerische Mathematik (2021).
[57] C. S. Kulkarni, P. F. J. Lermusiaux, Persistent rigid sets in realistic fluid flows using flow map composition, Ocean ModellingIn preparation (2020).
[58] C. S. Kulkarni, Prediction, analysis, and learning of advective transport in dynamic fluid flows, Ph.D. thesis, Massachusetts Institute of Technology, Department of Mechanical Engineering, Cambridge, Massachusetts (Sep. 2020).
[59] G. Froyland, K. Padberg, Almost-invariant and finite-time coherent sets: directionality, duration, and diffusion, in: Ergodic Theory, Open Dynamics, and Coherent Structures, Springer, 2014, pp. 171–216.
[60] F. Feppon, P. F. J. Lermusiaux, A geometric approach to dynamical model-order reduction, SIAM Journal on Matrix Analysis and Applications 39 (1) (2018) 510–538. doi:10.1137/16M1095202.
[61] C. S. Kulkarni, P. F. J. Lermusiaux, Advection without compounding errors through flow map composition, Journal of Computational Physics 398 (2019) 108859. doi:10.1016/j.jcp.2019.108859.
[62] R. Dautray, J.-L. Lions, Mathematical Analysis and Numerical Methods for Science and Technology, Springer Science Business Media, 2000. doi:10.1007/978-3-642-58004-8.
URL http://dx.doi.org/10.1007/978-3-642-58004-8
[63] M. C. Delfour, J.-P. Zolésio, Shapes and geometries: metrics, analysis, differential calculus, and optimization, Vol. 22, Siam, 2011.
[64] R. J. DiPerna, P.-L. Lions, Ordinary differential equations, transport theory and Sobolev spaces, Inventiones mathematicae 98 (3) (1989) 511–547.
[65] F. Boyer, Trace theorems and spatial continuity properties for the solutions of the transport equation, Differential and integral equations 18 (8) (2005) 891–934.
[66] G. Froyland, O. Junge, On fast computation of finite-time coherent sets using radial basis functions, Chaos: An Interdisciplinary Journal of Nonlinear Science 25 (8) (2015) 087409.
[67] G. Allaire, Analyse numérique et optimisation: Une introduction à la modélisation mathématique et à la simulation numérique, Editions Ecole Polytechnique, 2005.

[68] L. N. Trefethen, D. Bau III, Numerical linear algebra, Vol. 50, Siam, 1997.
[69] G. H. Golub, C. F. Van Loan, Matrix computations. 1996, Johns Hopkins University, Press, Baltimore, MD, USA (1996) 374–426.
[70] H. Brezis, Functional analysis, Sobolev spaces and partial differential equations, Springer Science & Business Media, 2010.
[71] G. Froyland, O. Junge, P. Koltai, Estimating long-term behavior of flows without trajectory integration: The infinitesimal generator approach, SIAM Journal on Numerical Analysis 51 (1) (2013) 223–247.
[72] R. Shapiro, Linear filtering, Mathematics of Computation 29 (132) (1975) 1094–1094.
[73] P. F. J. Lermusiaux, Error subspace data assimilation methods for ocean field estimation: theory, validation and applications, Harvard University, 1997.
[74] R. Shapiro, Smoothing, filtering, and boundary effects, Rev. Geophys. 8 (2) (1970) 359.
[75] P. F. J. Lermusiaux, F. Lekien, Dynamics and Lagrangian coherent structures in the ocean and their uncertainty, in: J. E. Marsden, J. Scheurle (Eds.), Extended Abstract in report of the Dynamical System Methods in Fluid Dynamics Oberwolfach Workshop, Mathematisches Forschungsinstitut Oberwolfach, Germany, 2005, p. 2. doi:10.1121/1.2988093.
[76] P. F. J. Lermusiaux, C.-S. Chiu, G. G. Gawarkiewicz, P. Abbot, A. R. Robinson, R. N. Miller, P. J. Haley, Jr, W. G. Leslie, S. J. Majumdar, A. Pang, F. Lekien, Quantifying uncertainties in ocean predictions, Oceanography 19 (1) (2006) 92–105. doi:10.5670/oceanog.2006.93.
[77] P. F. J. Lermusiaux, Uncertainty estimation and prediction for interdisciplinary ocean dynamics, Journal of Computational Physics 217 (1) (2006) 176–199. doi:10.1016/j.jcp.2006.02.010.
[78] F. Feppon, P. F. J. Lermusiaux, Dynamically orthogonal numerical schemes for efficient stochastic advection and Lagrangian transport, SIAM Review 60 (3) (2018) 595–625. doi:10.1137/16M1109394.
[79] C. S. Kulkarni, P. J. Haley, Jr., P. F. J. Lermusiaux, A. Dutt, A. Gupta, C. Mirabito, D. N. Subramani, S. Jana, W. H. Ali, T. Peacock, C. M. Royo, A. Rzeznik, R. Supekar, Real-time sediment plume modeling in the Southern California Bight, in: OCEANS Conference 2018, IEEE, Charleston, SC, 2018. doi:10.1109/OCEANS.2018.8653642.
[80] J. H. Bettencourt, C. López, E. Hernández-García, Oceanic three-dimensional lagrangian coherent structures: A study of a mesoscale eddy in the benguela upwelling region, Ocean Modelling 51 (2012) 73–83.
[81] D. G. Schmale III, S. D. Ross, Highways in the sky: Scales of atmospheric transport of plant pathogens, Annual review of phytopathology 53 (2015).
[82] P. J. Nolan, H. Foroutan, S. D. Ross, Pollution transport patterns obtained through generalized lagrangian coherent structures, Atmosphere 11 (2) (2020) 168.
[83] F. Beron-Vera, M. Olascoaga, An assessment of the importance of chaotic stirring and turbulent mixing on the west florida shelf, Journal of physical oceanography 39 (7) (2009) 1743–1755.
[84] S. V. Prants, M. Y. Uleysky, M. V. Budyansky, Lagrangian oceanography: large-scale transport and mixing in the ocean, Springer, 2017.
[85] C. S. Kulkarni, P. F. J. Lermusiaux, Learning Lagrangian transport features from Eulerian observations, In preparation (2020).

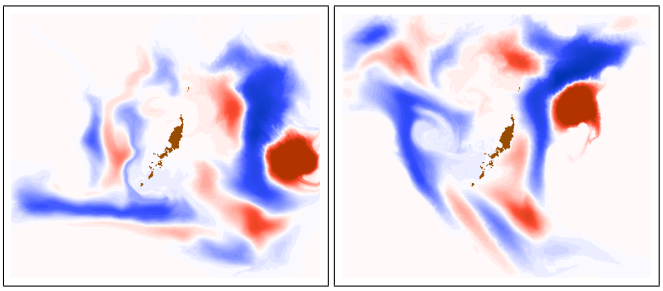

(a) $f_{3,\epsilon}$ (b) $g_{3,\epsilon}$

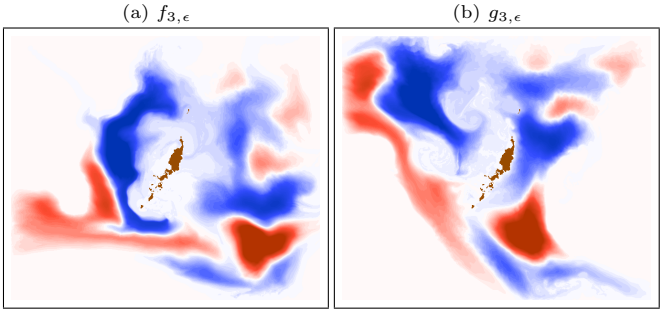

(c) $f_{7,\epsilon}$ (d) $g_{7,\epsilon}$

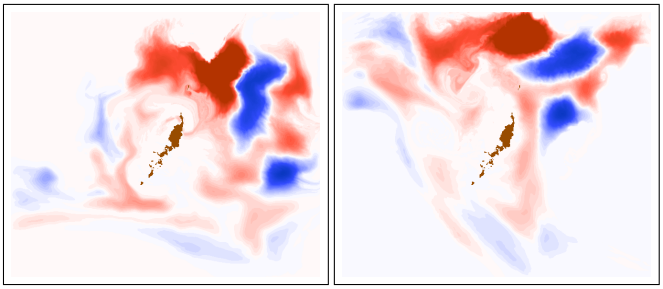

(e) $f_{12,\epsilon}$ (f) $g_{12,\epsilon}$

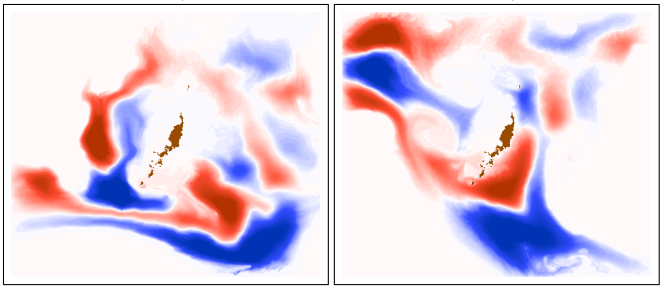

(g) $f_{17,\epsilon}$ (h) $g_{17,\epsilon}$

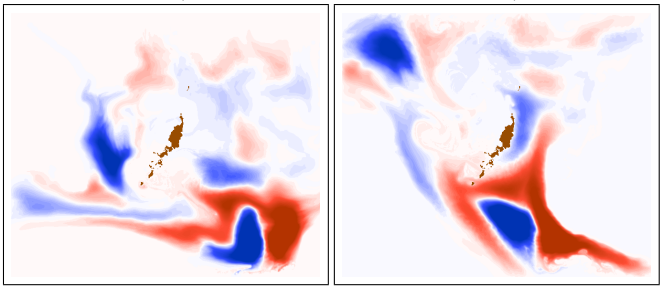

(i) $f_{20,\epsilon}$ (j) $g_{20,\epsilon}$

Figure 10: Approximate pairs of corresponding right and left singular vectors number 3, 7, 12, 17 and 20 of the diffusive operator $\boldsymbol{L}_\epsilon$ for the Palau Island flow of Section 2.3.